This article has been accepted for inclusion in a future issue of this journal. Content is final as presented, with the exception of pagination.

Tensor Completion Using Bilayer Multimode Low-Rank Prior and Total Variation

Haijin Zeng, *Graduate Student Member, IEEE*, Shaoguang Huang, *Member, IEEE*, Yongyong Chen, *Member, IEEE*, Sheng Liu, Hiêp Q. Luong, and Wilfried Philips, *Senior Member, IEEE*

***Abstract*— In this article, we propose a novel bilayer low-rankness measure and two models based on it to recover a low-rank (LR) tensor. The global low rankness of underlying tensor is first encoded by LR matrix factorizations (MFs) to the all-mode matricizations, which can exploit multiorientational spectral low rankness. Presumably, the factor matrices of all-mode decomposition are LR, since local low-rankness property exists in within-mode correlation. In the decomposed subspace, to describe the refined local LR structures of factor/subspace, a new low-rankness insight of subspace: a double nuclear norm scheme is designed to explore the so-called second-layer low rankness. By simultaneously representing the bilayer low rankness of the all modes of the underlying tensor, the proposed methods aim to model multiorientational correlations for arbitrary N-way ($N \geq 3$) tensors. A block successive upper-bound minimization (BSUM) algorithm is designed to solve the optimization problem. Subsequence convergence of our algorithms can be established, and the iterates generated by our algorithms converge to the coordinatewise minimizers in some mild conditions. Experiments on several types of public datasets show that our algorithm can recover a variety of LR tensors from significantly fewer samples than its counterparts.**

***Index Terms*— Bilayer low rank (LR), higher-order tensor, multimode decomposition, total variation (TV).**

I. Introduction

TENSOR is a generalization of vectors and matrices: a vector is a first-order or one-way tensor, and a matrix is a second-order tensor. The results of matrix completion have been successfully applied in various practical fields, such as inpainting, denoising, image batch alignment, keypoint/saliency detection, and affinity learning [1], [2], [3]. Tensor completion as a high-order extension of matrix completion has also aroused much research interest in recent years, due to higher-order tensor arises in many applications, for instance, video inpainting [4], magnetic resonance imaging (MRI) data recovery [5], 3-D image reconstruction [6], high-order web link analysis [16], and hyperspectral or multispectral data recovery [7].

Tensor completion (TC) is to recover the higher-order tensor with missing entries. Mathematically, this kind of problem can be modeled as follows:

$$\arg\min_{\mathcal{Y}} \operatorname{rank}(\mathcal{Y}) \quad \text{s.t. } \mathcal{P}_\Omega(\mathcal{Y}) = \mathcal{F} \tag{1}$$

where $\mathcal{Y} \in \mathbb{R}^{I_1 \times \cdots \times I_N}$ is the underlying Nth-order tensor; $\mathcal{F} \in \mathbb{R}^{I_1 \times \cdots \times I_N}$ is the observed data; Ω denotes the index set of observed entries, and $\mathcal{P}_\Omega$ keeps the entries in Ω and zeros out others (one can find more details of $\mathcal{P}_\Omega$ in Section II-C). Tensor is a high-dimensional extension of matrix; therefore, a natural processing method is to unfold or flatten the tensor into matrix and then use the matrix rank to describe the low-rank (LR) structure of the tensor, i.e.,

$$\arg\min_{\mathbf{Y}} \operatorname{rank}(\mathbf{Y}) \quad \text{s.t. } \mathcal{P}_\Omega(\mathcal{Y}) = \mathcal{F} \tag{2}$$

where $\mathbf{Y}$ is the matricization of $\mathcal{Y}$. Unfortunately, the rank minimization in (2) is generally an NP-hard problem. For effectively solving it, many methods relax the nonconvex rank function into the convex nuclear norm. Then, the optimization problem (2) can be rewritten as follows:

$$\arg\min_{\mathbf{Y}} \|\mathbf{Y}\|_* \quad \text{s.t. } \mathcal{P}_\Omega(\mathcal{Y}) = \mathcal{F} \tag{3}$$

where $\|\cdot\|_*$ denotes the nuclear norm of a matrix. Its solution is equivalent to the one of the models (2) under certain conditions. Equation (3) can be solved by fixed point continuation with approximate singular value decomposition (FPCA) [8], accelerated proximal gradient algorithm (APGL) [9], or the alternating direction method [10]. Although the above models can recover the LR tensor under certain conditions, they need to convert high-dimensional tensors into 2-D matrices. This strategy will lose high-dimensional structure information. For instance, the spectral dimension of hyperspectral images (HSIs) contains imaging results of the same spatial scene in different spectral bands, and there is high correlation between

Manuscript received 7 April 2022; revised 2 December 2022; accepted 8 April 2023. This work was supported in part by the Flemish Government (AI Research Program), UGent-Special Research Fund (BOF), National Natural Science Foundation of China under Grant 62106063, in part by the China Scholarship Council, Shenzhen Science and Technology Program under Grant RCBS20210609103708013, and in part by the "CUG Scholar" Scientific Research Funds at China University of Geosciences (Wuhan) under Grant 2022164. *(Corresponding author: Yongyong Chen.)*

Haijin Zeng, Hiêp Q. Luong, and Wilfried Philips are with the Image Processing and Interpretation Research Group, imec, Ghent University, 9000 Ghent, Belgium (e-mail: haijin.zeng@imec.be; hiep.luong@UGent.be; Wilfried.Philips@ugent.be).

Shaoguang Huang is with the School of Computer Science, China University of Geosciences, Wuhan 430074, China (e-mail: huangshaoguang@cug.edu.cn).

Yongyong Chen is with the School of Computer Science and Technology, Harbin Institute of Technology, Shenzhen 518055, China (e-mail: YongyongChen.cn@gmail.com).

Sheng Liu is with the School of Mathematical Sciences, University of Electronic Science and Technology of China, Chengdu 611731, China (e-mail: liusheng16@163.com).

Color versions of one or more figures in this article are available at https://doi.org/10.1109/TNNLS.2023.3266841.

Digital Object Identifier 10.1109/TNNLS.2023.3266841

2162-237X © 2023 IEEE. Personal use is permitted, but republication/redistribution requires IEEE permission.
See https://www.ieee.org/publications/rights/index.html for more information.

Authorized licensed use limited to: University of Gent. Downloaded on August 08,2023 at 08:45:04 UTC from IEEE Xplore. Restrictions apply.

This article has been accepted for inclusion in a future issue of this journal. Content is final as presented, with the exception of pagination.

the discrete spectral bands [7]; video often has multiple frames of images, and there is a temporal–spatial correlation between/inside the images of each frame [11].

Many studies [12], [13], [14], [15], [16], [17] have proven that completion methods directly modeling tensors could better preserve the high-dimensional structure information than the ones modeling the tensor matricization. In the literature, two common LR TC methods are LR tensor decomposition-based methods and tensor rank minimization-based methods, respectively. The former one generally decomposes the target tensor into a combination of several subtensors and matrices for recovering an LR tensor from its partially observed entries, e.g., weighted LR tensor decomposition method [18], Bayes-based framework [19], multilinear graph embedding [20], and tensor singular value decomposition (SVD) methods [16], [21], [22]. These methods can effectively recover tensors; however they are usually sensitive to a given rank, which is usually estimated based on the raw data.

The tensor rank minimization-based method is another widely studied method, and their robustness to noisy and missing data has also been proven. Therefore, they have been universally utilized in TC problems. Usually, they can be solved by replacing the rank function with its convex or nonconvex relaxations in the minimization problem. This type of method can significantly reduce the deviation of rank estimation (RE). A few notable examples are the CANDECOMP/PARAFAC rank minimization method [23], the Tucker rank minimization method [24], [25], tensor trains [26], the tensor nuclear norm (TNN)-based rank approximation methods [27], [28], [29], and various redefined rank approximation methods with varied relaxations [30], [31], [32]. Among these tensor rank minimization-based methods, the tensor SVD (t-SVD) [29]-based TNN, as the tightest convex surrogate of the tensor rank, has been widely used for LR TC [22], [33]. In addition, TNN has also been integrated with total variation (TV) and other transforms instead of fast Fourier transform (FFT) [34], [35]. Specifically, the TNN regularized TC model can be described as follows:

$$\arg\min_{\mathcal{Y}} \|\mathcal{Y}\|_{\text{TNN}} \quad \text{s.t. } \mathcal{P}_\Omega(\mathcal{Y}) = \mathcal{F} \tag{4}$$

where $\|\cdot\|_{\text{TNN}}$ is the TNN of a tensor. For a third-order tensor $\mathcal{A} \in \mathbb{R}^{n_1\times n_2\times n_3}$ and its FFT along the third dimension $\bar{\mathcal{A}} = \text{fft}(\mathcal{A}, [], 3)$, the TNN of $\mathcal{A}$ is defined as the average of the nuclear norm of all the frontal slices in $\bar{\mathcal{A}}$, i.e., $\|\mathcal{A}\|_{\text{TNN}} := (1/n_3)\sum_{i=1}^{n_3}\|\bar{\mathbf{A}}^{(i)}\|_*$, where $\bar{\mathbf{A}}^{(i)}$ denotes the ith frontal slice of $\bar{\mathcal{A}}$.

Furthermore, to alleviate the RE issue and bias phenomena of the TNN minimization, Shi et al. [36] design an RE-based TNN model, by simultaneously minimizing the reconstruction error and TNN of the equivalent f-diagonal tensor. Jiang et al. [37] propose a nonconvex surrogate of the tensor rank, i.e., a partial sum of the TNN (PSTNN). PSTNN regularized TC model can be written as follows:

$$\arg\min_{\mathcal{Y}} \|\mathcal{Y}\|_{\text{PSTNN}} \quad \text{s.t. } \mathcal{P}_\Omega(\mathcal{Y}) = \mathcal{F} \tag{5}$$

where $\|\cdot\|_{\text{PSTNN}}$ is the PSTNN of a tensor. For a third-order tensor $\mathcal{A} \in \mathbb{R}^{n_1\times n_2\times n_3}$, the PSTNN of $\mathcal{A}$ is defined as

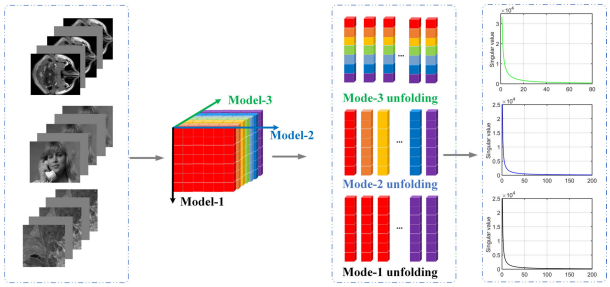


Fig. 1. LR properties of tensor mode-n unfoldings.

$\|\mathcal{A}\|_{\text{PSTNN}} := (1/n_3)\sum_{i=1}^{n_3}\|\bar{\mathbf{A}}^{(i)}\|_{p=M}$, where $\|\bar{\mathbf{A}}^{(i)}\|_{p=M} := \sum_{j=M+1}^{\min(n_1,n_2)}\sigma_j(\bar{\mathbf{A}}^{(i)})$; $\sigma_j(\bar{\mathbf{A}}^{(i)})(j = 1, \ldots, \min(n_1, n_2))$ denotes the jth largest singular value of $\bar{\mathbf{A}}^{(i)} \in \mathbb{C}^{n_1\times n_2}$.

Although the abovementioned LR TC studies show great success in dealing with various issues, three major open questions have yet to be addressed. First, the above approaches only utilize the LR prior lying in one mode of the underlying tensor. They ignore the prior knowledge of close multilinear interactions among multiple dimensions of a given tensor object. One can see an example in Fig. 1. It is obvious that all the three modes of real tensor data have similar LR properties. Second, TNN-based methods [22], [37] need to compute lots of SVDs, which become very slow or even not applicable for large-scale problems [38]. Third, all these methods adopt single nuclear norm or partial sum minimization of singular values norm, which would cause suboptimal solution of the LR-based problem.

This article presents answers to those questions. Motivated and convinced by the promising performance of models that utilize the low rankness in all modes of tensors [27], [38], we formulate a bilayer LR measure to represent the high-dimensional correlation among all modes of the underlying tensors. Specifically, we design the first LR layer by applying parallel LR matrix factorization (MF) to each mode of the tensor, to utilize the mode-n LR prior (as shown in Fig. 1). Then, as the LR structure of all modes is implicitly included in the LR factorization, we bundle up the second LR layer by employing double nuclear norm regularization to characterize the underlying joint-manifold drawn from the mode factors, as shown in Fig. 2, and the proposed model-1 is formulated as follows:

$$\begin{aligned}&\arg\min_{\mathcal{Y},\mathbf{X}_n,\mathbf{A}_n}\sum_{n=1}^{N}(\tau_n\|\mathbf{X}_n\|_* + \lambda_n\|\mathbf{A}_n\|_*)\\ &\text{s.t. } \mathcal{P}_\Omega(\mathcal{Y}) = \mathcal{F}, \quad \mathbf{Y}_{(n)} = \mathbf{A}_n\mathbf{X}_n, \quad n = 1, 2, \ldots, N\end{aligned} \tag{6}$$

where τ_n and λ_n are positive parameters; $\mathbf{A}_n \in \mathbb{R}^{r_n\times\Pi_{j\neq n}I_j}$ represents a library (each column contains a signature of the nth-mode direction), and $\mathbf{X}_n \in \mathbb{R}^{I_n\times r_n}$ is called an encoding. For example, in the unmixing problem for HSIs [39], each column of $\mathbf{A}_3$ denotes a spectral signature, and each row of $\mathbf{X}_3$ denotes the fractional abundances of a given spectral signature. This interpretation is also valid for the mode-3 factorization of videos and MRIs. The proposed bilayer LR measure encodes the auxiliary factor information in addition to the direct LR decomposition of the original tensor in all

Authorized licensed use limited to: University of Gent. Downloaded on August 08,2023 at 08:45:04 UTC from IEEE Xplore. Restrictions apply.

This article has been accepted for inclusion in a future issue of this journal. Content is final as presented, with the exception of pagination.

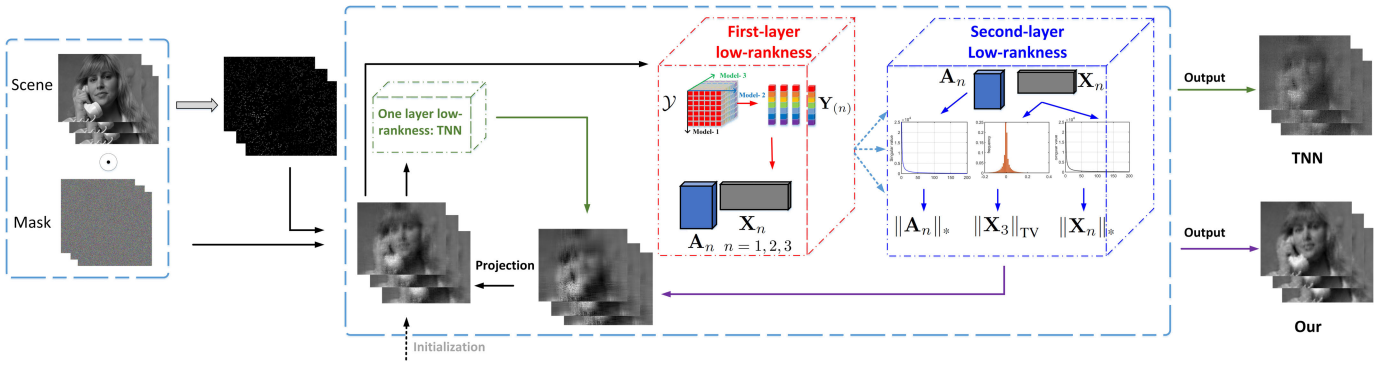


Fig. 2. Image formation process of the proposed TC algorithm, i.e., one layer low-rankness-based TNN and the reconstruction process using the proposed enhanced bilayer prior algorithm. The real data shown in the figure are Suzie, and the sampling rate is 5%.

orientations, integrating the measure metric of LR decomposition with LR approximation. It estimates the mode factors and missing entries accurately by employing these additional insights prior knowledge, as to be seen in the right outputs of Fig. 2, and our multimodes-based mode preserves much more detail than the single-mode-based TNN.

Furthermore, to consider the inner geometric structure of data space, we use TV (see Section II-B) regularization to construct the global relationship of real tensor data, and propose our model-2 as follows:

$$\begin{aligned} &\arg\min_{\mathcal{Y},\mathbf{X}_n,\mathbf{A}_n} \sum_{n=1}^{N} (\tau_n \|\mathbf{X}_n\|_* + \lambda_n \|\mathbf{A}_n\|_*) + \mu \|\mathbf{X}_3\|_{\mathrm{TV}} \\ &\text{s.t. } \mathcal{P}_\Omega(\mathcal{Y}) = \mathcal{F}, \quad \mathbf{Y}_{(n)} = \mathbf{A}_n \mathbf{X}_n, \quad n = 1, 2, 3, \ldots, N \end{aligned} \tag{7}$$

where μ is a positive parameter. It is worth noting that the proposed model can fully capture all modes low rankness and piecewise smooth prior of the underlying tensor, and, thus, is expected to have a strong ability of LR TC. Moreover, both of our bilayer LR measure are generic to the all modes of underlying n-way tensor, since they do not rely on the use of one mode-specific LR prior. It can, therefore, be applied to any LR tensor data, i.e., to a very wide class of problems in image processing and computer vision. For the other details of the models, we ask for the reader's patience until Section III.

The contributions of this article are listed as follows.

1) We propose two novel bilayer LR models to recover an LR tensor. By designing a bilayer LR measure, the proposed models represent the global LR prior more faithfully and also take into account the additional internal LR features along all modes. It can also be used to replace the conventional LR measure to improve the performance of general high-dimensional signal processing models.
2) To represent the local smoothness of underlying tensor datasets and preserve edges, we integrate TV to the proposed bilayer measure and apply them to LR tensor completion.
3) A block successive upper-bound minimization (BSUM) algorithm is designed to solve the optimization problem. Subsequence convergence of our algorithms is established, and the iterates generated by our algorithms converge to the coordinatewise minimizers in some mild conditions.
4) Several experiments of 3-D gray video, 4-D color video, MRI and HSI completion, inpainting, and destriping are implemented. The comprehensive results confirmed that the proposed algorithm can recover a variety of LR tensors from significantly fewer samples than the testing TC methods.

II. Preliminary

Before introducing our models and their algorithms, we review some related notations, tensor operations, regularizers, and operators.

A. Notations

Following [38], vectors are denoted as bold lowercase letters, e.g., $\mathbf{x}$, $\mathbf{y}$; matrices are denoted as bold uppercase letters, e.g., $\mathbf{X}$, $\mathbf{Y}$, and tensors are denoted as calligraphy letters, e.g., $\mathcal{X}, \mathcal{Y}$. Let $x_{i_1,\ldots,i_N}$ represent the $(i_1, \ldots, i_N)$th component of an Nth-order tensor $\mathcal{X}$. Then, for $\mathcal{X}, \mathcal{Y} \in \mathbb{R}^{I_1 \times \cdots \times I_N}$, their inner product is defined as follows:

$$\langle \mathcal{X}, \mathcal{Y} \rangle = \sum_{i_1=1}^{I_1} \cdots \sum_{i_N=1}^{I_N} x_{i_1,\ldots,i_N} y_{i_1,\ldots,i_N}. \tag{8}$$

Based on the inner product, one can define the **Frobenius norm** of a tensor $\mathcal{X}$ as $\|\mathcal{X}\|_{\mathrm{F}} = (\langle \mathcal{X}, \mathcal{X} \rangle)^{1/2}$. **Fiber** of tensor $\mathcal{X}$ is defined as a vector obtained by fixing all indices of $\mathcal{X}$ except one, and **Slice** of $\mathcal{X}$ is defined as a matrix by fixing all indices of $\mathcal{X}$ except two. The mode-n unfolding of $\mathcal{X}$ is denoted as a matrix $\mathbf{X}_{(n)} \in \mathbb{R}^{I_n \times \Pi_{j \neq n} I_j}$ with columns being the mode-n fibers of $\mathcal{X}$ in the lexicographical order.

To clearly represent the matricization process, we define $\mathrm{unfold}_n(\mathcal{X}) = \mathbf{X}_{(n)}$, and fold_n is the inverse of unfold_n, i.e., $\mathrm{fold}_n(\mathrm{unfold}_n(\mathcal{X})) = \mathcal{X}$. Let $\mathrm{rank}_n(\mathcal{X}) = \mathrm{rank}(\mathbf{X}_{(n)})$ denote the n-rank of $\mathcal{X}$. Then, the rank of $\mathcal{X}$ is defined as an array $\mathrm{rank}(\mathcal{X}) = (\mathrm{rank}(\mathbf{X}_{(1)}), \ldots, \mathrm{rank}(\mathbf{X}_{(N)}))$.

B. Total Variation

In (7), $\mathbf{X}_3^{(i,k)} \in \mathbb{R}^{1 \times I_1 I_2}$ denotes a vector by lexicographically ordering the entries of the matrix $\mathcal{X}(:, :, k, i_4, \ldots, i_N) \in \mathbb{R}^{I_1 \times I_2}$, which is a slice of the tensor $\mathcal{X}$, where $i = 1 + \sum_{p=4}^{N}$

Authorized licensed use limited to: University of Gent. Downloaded on August 08,2023 at 08:45:04 UTC from IEEE Xplore. Restrictions apply.

This article has been accepted for inclusion in a future issue of this journal. Content is final as presented, with the exception of pagination.

$(i_p - 1)J_p$ and $J_p = \Pi_{m=4}^{p-1} I_m$

$$\mathcal{X} = \text{fold}_3(\mathbf{X}_3) \in \mathbb{R}^{I_1 \times I_2 \times r_3 \times I_4 \times \cdots \times I_N}.$$

Then, the isotropic TV [40] is defined as follows:

$$\|\mathbf{X}_3\|_{\text{TV}} := \sum_{k=1}^{\hat{s}} \sum_{i=1}^{r_3} \sum_{j=1}^{I_1 I_2} \sqrt{\left|\tilde{\mathbf{D}}_{j,1} \mathbf{X}_3^{(i,k)}\right|^2 + \left|\tilde{\mathbf{D}}_{j,2} \mathbf{X}_3^{(i,k)}\right|^2} \quad (9)$$

where $\hat{s} = \prod_{i=4}^{N} I_i$; $\mathbf{X}_3^{(i,k)}$ represents the kth block of ith row of $\mathbf{X}_3$, and $\tilde{\mathbf{D}}_{j,1}$ and $\tilde{\mathbf{D}}_{j,2}$ represent the discrete gradient operators at the first- and second-mode directions, respectively. Following the representation of $\tilde{\mathbf{D}}$, $\tilde{\mathbf{D}}_{j,1}\mathbf{X}_3^{(i,k)}$ denotes the gradient values of $\mathbf{X}_3^{(i,k)}$ at the first-mode directions, and $\tilde{\mathbf{D}}_{j,2}\mathbf{X}_3^{(i,k)}$ denotes the gradient values of $\mathbf{X}_3^{(i,k)}$ at the second-mode direction of the jth pixel in $\mathbf{X}_3^{(i,k)}$.

C. Operators

The proximal operator of a given convex function $f(x)$ is defined as follows:

$$\text{prox}_f(x, y) := \arg\min_x f(x) + \frac{\rho}{2}\|x - y\|^2 \quad (10)$$

where ρ is a positive constant. The problem $\arg\min_x\{f(x)\}$ is equivalent to $\arg\min_{x,y}\{f(x) + (\rho/2)\|x - y\|^2\}$. Thus, one can obtain the minimization of $f(x)$ by iteratively solving $\text{prox}_f(x, x^k)$, where x^k is the latest update of x. The highlight of the proximal operator is that it can guarantee the strong convexity of objective function (10), as long as $f(x)$ is convex.

Let Ω be the index set of observed entries; then, the projection operator $\mathcal{P}_\Omega$ keeps the entries in Ω and zeros out others, i.e.,

$$(\mathcal{P}_\Omega(\mathcal{Y}))_{i_1,\ldots,i_N} = \begin{cases} y_{i_1,\ldots,i_N}, & (i_1, \ldots, i_N) \in \Omega \\ 0, & \text{otherwise.} \end{cases} \quad (11)$$

Then, the singular value thresholding (SVT) operator [41] is defined as follows. Supposing $\mathbf{M}$ is a matrix of size $I_1 I_2 \times I_3$, and the singular value of matrix $\mathbf{M}$ of rank r is decomposed into

$$\mathbf{M} = \mathbf{P}\mathbf{E}_r\mathbf{Q}^*, \quad \mathbf{E}_r = \text{diag}\big(\{\sigma_i\}_{1 \le i \le r}\big).$$

The singular value shrinkage operator then obeys

$$\text{SH}_\delta(\mathbf{M}) = \arg\min_{\text{rank}(\mathbf{X}) \le r} \delta\|\mathbf{X}\|_* + \frac{1}{2}\|\mathbf{X} - \mathbf{W}\|_{\text{F}}^2$$

where

$$\text{SH}_\delta(\mathbf{W}) = \mathbf{P}\,\text{diag}\{\max((\sigma_i - \delta), 0)\}\mathbf{Q}^*. \quad (12)$$

III. Proposed Models and Algorithms

A. Proposed Models

The objective function of our model-1 (6) is

$$f(\mathbf{X}, \mathbf{A}, \mathcal{Y}) = \sum_{n=1}^{N} \left(\frac{\alpha_n}{2} \left\|\mathbf{Y}_{(n)} - \mathbf{A}_n\mathbf{X}_n\right\|_{\text{F}}^2 + \tau_n\|\mathbf{X}_n\|_* + \lambda_n\|\mathbf{A}_n\|_* \right) \quad (13)$$

where the values of $\alpha_n, n = 1, 2, \ldots, N$, are positive weights satisfying $\sum_{n=1}^{N} \alpha_n = 1$. Also, the objective function of our model-2 (7) is

$$f(\mathbf{X}, \mathbf{A}, \mathcal{Y}) = \sum_{n=1}^{N} \left(\frac{\alpha_n}{2} \left\|\mathbf{Y}_{(n)} - \mathbf{A}_n\mathbf{X}_n\right\|_{\text{F}}^2 + \tau_n\|\mathbf{X}_n\|_* + \lambda_n\|\mathbf{A}_n\|_* \right) + \mu\|\mathbf{X}_3\|_{\text{TV}}. \quad (14)$$

First, we explain why it is necessary to represent the LR property in all modes of underlying tensors. In an nth-order tensor, each order represents one factor and has its specific inherent structural properties. Therefore, each mode of the underlying tensor has specific prior information. Although a tensor could be composed of randomly arranged elements, it is usually assumed that the within-factor and joint-factor variations are known a prior and can be regarded as auxiliary information [20]. For example, a video object is a third-order tensor with variations spanned by the rows, columns, and time axis. Even when the value of an element is unknown, we may reasonably infer that adjacent rows, columns, or frames are highly correlated. This is because the local similarity of visual data usually exists in within-factor relations (e.g., among adjacent rows, columns, or frames) or joint-factor relations (e.g., between spatially adjacent and temporally adjacent pixels). See Fig. 1 for an illustration of real third-order tensor data. It is obviously seen that the singular value curves of their three modes decay rapidly; that is to say that, only a small part of the singular values are greater than zero. Therefore, the three modes of the real tensor data have the similar LR property.

Actually, this phenomenon has specific physical meaning. Taking the HSI $\mathcal{Y} \in \mathbb{R}^{m \times n \times p}$ for an example, it is well known that each spectral characteristic can be represented by a linear combination of a small number of pure spectral endmembers. It means that its mode-3 matricization $\mathbf{Y}_{(3)}$ can be decomposed into $\mathbf{Y}_{(3)} = \mathbf{A}_3\mathbf{X}_3$, where $\mathbf{A}_3 \in \mathbb{R}^{p \times r}$ is the so-called endmember matrix, and $\mathbf{X}_3 \in \mathbb{R}^{r \times mn}$ is regarded as the abundance matrix. As described in [42], the number of endmembers r is relatively small, i.e., $r \ll p$ or $r \ll mn$. That is to say that, only a small part of the singular values are greater than zero, as shown in the fourth column of Fig. 1. Based on the above practical physical meaning, we utilize the LR prior lying in all modes of underlying tensors to promote the performance of TC models.

Second, we explain why we employ the double nuclear norms of $\mathbf{A}_n$ and $\mathbf{X}_n$ to represent the LR prior in each mode. Without increasing the computational complexity, we first unfold the tensor among all modes; then, each mode-n unfolding matrix is decomposed into two smaller factor matrices [38], i.e., $\mathbf{Y}_{(n)} = \mathbf{A}_n\mathbf{X}_n$, $n = 1, 2, \ldots, N$. The LR structure of tensors not only is inherited by the factor matrices, i.e., $\mathbf{A}_n$, $\mathbf{X}_n$, but also can be represented more sufficiently. Then, we add the double nuclear norm regularization to the factor matrices for characterizing the underlying joint-manifold drawn from the mode factors. By exploiting this auxiliary information, our method leverages two classic schemes and accurately estimates the model factors and missing entries. Unfortunately, it is difficult to directly calculate the nuclear norm of the product of

Authorized licensed use limited to: University of Gent. Downloaded on August 08,2023 at 08:45:04 UTC from IEEE Xplore. Restrictions apply.

This article has been accepted for inclusion in a future issue of this journal. Content is final as presented, with the exception of pagination.

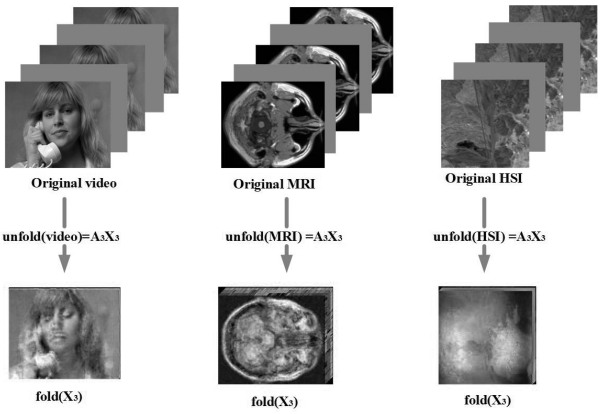


Fig. 3. Illustration of the structural characteristics of $\mathbf{X}_3$.

two matrices, i.e., $\|\mathbf{Y}_{(n)}\|_* = \|\mathbf{A}_n\|_*\|\mathbf{X}_n\|_*, n = 1, 2, 3, \ldots, N$. Therefore, according to the fundamental inequality, we reformulate the product of two nuclear norms into

$$\begin{aligned}\arg\min_{\mathbf{Y}_{(n)}}\left\|\mathbf{Y}_{(n)}\right\|_* &= \arg\min_{\mathbf{Y}_{(n)}=\mathbf{A}_n\mathbf{X}_n}\|\mathbf{A}_n\|_*\|\mathbf{X}_n\|_* \\ &= \arg\min_{\mathbf{Y}_{(n)}=\mathbf{A}_n\mathbf{X}_n}\left(\frac{1}{2}(\|\mathbf{A}_n\|_* + \|\mathbf{X}_n\|_*)\right)^2. \quad (15)\end{aligned}$$

Third, we explain why we integrate the TV regularization of $\mathbf{X}_3$ into the proposed LR TC model. Actually, TV regularization measures the difference between a pixel and its neighbors; the smaller the difference is, the better the TV regularization plays. For image data, e.g., video, MRI, and HSI, their piecewise smoothness always be shown spatially, i.e., the first-mode (horizontal) and the second-mode (vertical) directions. It means that the difference between the pixel of $\mathbf{X}_n$ and its first- and second-mode direction neighbors is small. Thus, we can introduce the TV regularization of $\mathbf{X}_n$ at the first- and second-mode directions into the proposed tensor completion model. However, $\mathbf{X}_1$ and $\mathbf{X}_2$ do not contain the complete information of the first and second modes for $\mathcal{Y}$, because the rank of $\mathbf{Y}_{(1)}$ is $r_1(r_1 < I_1)$; that is, the dimension of the corresponding tensor is $r_1 \times I_2 \times \cdots \times I_N$ [40]. Thus, we introduce the TV regularization of $\mathbf{X}_{n_0}, n_0 \in \{3, 4, \ldots, N\}$. Without loss of generality, we adopt the TV regularization of $\mathbf{X}_3$. For three types of public tensor datasets, we show the specific structure of their $\mathbf{X}_3$ in Fig. 3. As shown in Fig. 3, $\mathbf{X}_3$ has an obvious smooth structure, so it is appropriate to use TV to explore the inherent structure prior of $\mathbf{X}_3$.

B. Proposed Algorithms

The proposed model-1 (6) and model-2 (7) are two complicated optimization problems, which are difficult to solve directly. Here, we adopt the BSUM [43] to solve them.

According to the proximal operator (10), the update can be written as follows:

$$\text{Prox}_f(\mathcal{S}, \mathcal{S}^k) = \arg\min_{\mathcal{S}} f(\mathcal{S}) + \frac{\rho}{2}\|\mathcal{S} - \mathcal{S}^k\|_{\text{F}}^2 \quad (16)$$

where $\rho > 0$ is the proximal parameter, $\mathcal{S} = (\mathbf{X}, \mathbf{A}, \mathcal{Y})$, and $\mathcal{S}^k = (\mathbf{X}^k, \mathbf{A}^k, \mathcal{Y}^k)$. Let $S_1^k = (\mathbf{X}^k, \mathbf{A}^k, \mathcal{Y}^k)$, $S_2^k = (\mathbf{X}^{k+1}, \mathbf{A}^k, \mathcal{Y}^k)$, and $S_3^k = (\mathbf{X}^{k+1}, \mathbf{A}^{k+1}, \mathcal{Y}^k)$. By BSUM, (16) can be rewritten as follows:

$$\begin{cases}\mathbf{X}^{k+1} = \arg\min_{\mathbf{X}} f(\mathbf{X}, \mathbf{A}^k, \mathcal{Y}^k) + \frac{\rho}{2}\|\mathbf{X} - \mathbf{X}^k\|_{\text{F}}^2 \\ \mathbf{A}^{k+1} = \arg\min_{\mathbf{A}} f(\mathbf{X}^{k+1}, \mathbf{A}, \mathcal{Y}^k) + \frac{\rho}{2}\|\mathbf{A} - \mathbf{A}^k\|_{\text{F}}^2 \\ \mathcal{Y}^{k+1} = \arg\min_{\mathcal{Y}} f(\mathbf{X}^{k+1}, \mathbf{A}^{k+1}, \mathcal{Y}) + \frac{\rho}{2}\|\mathcal{Y} - \mathcal{Y}^k\|_{\text{F}}^2\end{cases} \quad (17)$$

i.e.,

$$\begin{cases}\mathbf{X}^{k+1} = \text{Prox}_f(\mathbf{X}, \mathcal{S}_1^k) \\ \mathbf{A}^{k+1} = \text{Prox}_f(\mathbf{A}, \mathcal{S}_2^k) \\ \mathcal{Y}^{k+1} = \text{Prox}_f(\mathcal{Y}, \mathcal{S}_3^k).\end{cases} \quad (18)$$

1) Update $\mathbf{X}_n$ With Fixing Others: To efficiently solve $\mathbf{X}_n$ subproblem in (18), we first introduce one auxiliary variable $\mathbf{X}_n = \mathbf{Z}_n$. Then, $\mathbf{X}_n$ subproblem can be rewritten as follows:

$$\begin{aligned}\arg\min_{\mathbf{X}_n, \mathbf{Z}_n}\sum_{n=1}^{N}\Big(&\frac{\alpha_n}{2}\|\mathbf{Y}_{(n)} - \mathbf{A}_n\mathbf{X}_n\|_{\text{F}}^2 + \tau_n\|\mathbf{Z}_n\|_* \\ &+ \frac{\rho_n}{2}\|\mathbf{X}_n - \mathbf{X}_n^k\|_{\text{F}}^2 + \langle\Gamma_n^{\mathbf{X}}, \mathbf{X}_n - \mathbf{Z}_n\rangle \\ &+ \frac{\rho_n}{2}\|\mathbf{X}_n - \mathbf{Z}_n\|_{\text{F}}^2\Big) + \mu\|\mathbf{X}_3\|_{\text{TV}} \quad (19)\end{aligned}$$

where $\Gamma_n^{\mathbf{X}}$ is a Lagrange multiplier. With other variables fixed, the minimization subproblem for $\mathbf{Z}_n$ can be deduced from (19) as follows:

$$\mathbf{Z}_n^{k+1} = \arg\min_{\mathbf{Z}_n}\tau_n\|\mathbf{Z}_n\|_* + \frac{\rho_n}{2}\|\mathbf{X}_n^k - \mathbf{Z}_n + \Gamma_n^{\mathbf{X}}/\rho_n\|_{\text{F}}^2. \quad (20)$$

By using the SVT operator (12), it is easy to get

$$\mathbf{Z}_n^{k+1} = \text{SH}_{\frac{\tau_n}{\rho_n}}(\mathbf{X}_n^k + \Gamma_n^{\mathbf{X}}/\rho_n), \quad n = 1, 2, \ldots, N. \quad (21)$$

Based on the augmented lagrange multiplier (ALM) method, the multipliers are updated by the following equations:

$$\Gamma_n^{\mathbf{X}} = \Gamma_n^{\mathbf{X}} + \mathbf{X}_n - \mathbf{Z}_n. \quad (22)$$

With other variables fixed, the minimization subproblem for $\mathbf{X}_n (n \neq 3)$ can be deduced from (19) as follows:

$$\begin{aligned}\mathbf{X}_n^{k+1} = \arg\min_{\mathbf{X}_n}&\frac{\alpha_n}{2}\|\mathbf{Y}_{(n)} - \mathbf{A}_n^k\mathbf{X}_n\|_{\text{F}}^2 \\ &+ \frac{\rho_n}{2}\left\|\mathbf{X}_n - \frac{\mathbf{Z}_n^{k+1} - \Gamma_n^k/\mu_n + \mathbf{X}_n^k}{2}\right\|_{\text{F}}^2. \quad (23)\end{aligned}$$

They are convex and have the following closed-form solutions:

$$\begin{aligned}\mathbf{X}_n^{k+1} = \left(\alpha_n\mathbf{A}_n^T\mathbf{A}_n + 2\rho\mathbf{I}_n\right)^{-1}\Bigg[&\alpha_n\mathbf{A}_n^T\mathbf{Y}_{(n)} \\ &+ \mu_n\left(\frac{\mathbf{Z}_n^{k+1} - \Gamma_n^k/\mu_n + \mathbf{X}_n^k}{2}\right)\Bigg]. \quad (24)\end{aligned}$$

With other variables fixed, the minimization subproblem for $\mathbf{X}_3$ can be deduced from (19) as follows:

$$\begin{aligned}\mathbf{X}_3^{k+1} = \arg\min_{\mathbf{X}_3}&\frac{\alpha_3}{2}\|\mathbf{Y}_{(3)} - \mathbf{A}_3^k\mathbf{X}_3\|_{\text{F}}^2 \\ &+ \frac{\rho_3}{2}\left\|\mathbf{X}_3 - \frac{\mathbf{Z}_3^{k+1} - \Gamma_3^k/\mu_3 + \mathbf{X}_3^k}{2}\right\|_{\text{F}}^2 + \mu\|\mathbf{X}_3\|_{\text{TV}}. \quad (25)\end{aligned}$$

Compared with the optimization problem of $X_n, n \neq 3$, the optimization problem of $\mathbf{X}_3$ has an additional TV regular term

Authorized licensed use limited to: University of Gent. Downloaded on August 08,2023 at 08:45:04 UTC from IEEE Xplore. Restrictions apply.

This article has been accepted for inclusion in a future issue of this journal. Content is final as presented, with the exception of pagination.

imposed on $\mathbf{X}_3$. It can be solved efficiently using alternating direction method of multipliers (ADMM) [40], [44], [45]. To obtain the closed solution of (25), we denote $\hat{\mathbf{X}}$ as the transpose of $\mathbf{X}$. Then, the solution of (25) is equivalent to one of the following minimization problems:

$$\hat{\mathbf{X}}_3^{k+1} = \arg\min_{\hat{\mathbf{X}}_3} \frac{1}{2}\left\|\hat{\mathbf{Y}}_{(3)}^k - \hat{\mathbf{X}}_3\hat{\mathbf{A}}_3^k\right\|_{\mathrm{F}}^2 + \frac{\rho}{2}\left\|\hat{\mathbf{X}}_3 - \frac{\hat{\mathbf{Z}}_3^{k+1} - \hat{\Gamma}_3^k/\mu_3 + \hat{\mathbf{X}}_3^k}{2}\right\|_{\mathrm{F}}^2 + \mu\left\|\hat{\mathbf{X}}_3\right\|_{\mathrm{TV}} \quad (26)$$

where $\rho = (\rho_3/\alpha_3)$. For simplicity, let $\hat{\mathbf{O}}_3^k = ((\hat{\mathbf{Z}}_3^{k+1} - \hat{\Gamma}_3^k/\mu_3 + \hat{\mathbf{X}}_3^k)/2)$. Then, we introduce two auxiliary variables and convert (26) into

$$\begin{aligned}\arg\min_{\hat{\mathbf{X}}_3,\mathbf{U}} \mu\sum_{i=1}^{s_3}\sum_{j=1}^{r_3}\left\|\mathbf{U}_{i,j}\right\|_2 + \frac{1}{2}\left\|\tilde{\mathbf{Y}}_{(3)}^k - \hat{\mathbf{X}}_3\hat{\mathbf{A}}_3^k\right\|_{\mathrm{F}}^2 \\ + \frac{\rho}{2}\left\|\hat{\mathbf{X}}_3 - \hat{\mathbf{O}}_3^k\right\|_{\mathrm{F}}^2 \\ \text{s.t. } \mathbf{U}_1 = \mathbf{D}_1\hat{\mathbf{X}}_3, \quad \mathbf{U}_2 = \mathbf{D}_2\hat{\mathbf{X}}_3 \end{aligned} \quad (27)$$

where $\mathbf{U}_{i,j} = [(\mathbf{U}_1)_{i,j}, (\mathbf{U}_2)_{i,j}] \in \mathbb{R}^{1\times 2}$; $(\mathbf{U}_1)_{i,j}$ and $(\mathbf{U}_2)_{i,j}$ denote the (i, j)th entries of $\mathbf{U}_1$ and $\mathbf{U}_2$, respectively; $\mathbf{D}_t := \mathrm{Diag}(\tilde{\mathbf{D}}_t, \tilde{\mathbf{D}}_t, \ldots, \tilde{\mathbf{D}}_t)$, $t = 1, 2$; and $\tilde{\mathbf{D}}_1$ and $\tilde{\mathbf{D}}_2$ are, respectively, the assembled first-order difference matrices in the first- and second-mode directions based on $\tilde{\mathbf{D}}_{j,1}$ and $\tilde{\mathbf{D}}_{j,2}$ in (9).

Problem (27) can be solved by solving two decoupled subproblems, which the convergence can be guaranteed [46]. By the ALM method, (27) can be rewritten as follows:

$$\begin{aligned}\arg\min_{\hat{\mathbf{X}}_3,\mathbf{U}} \frac{1}{2}\left\|\hat{\mathbf{Y}}_{(3)}^k - \hat{\mathbf{X}}_3\hat{\mathbf{A}}_3^k\right\|_{\mathrm{F}}^2 + \frac{\rho}{2}\left\|\hat{\mathbf{X}}_3 - \hat{\mathbf{O}}_3^k\right\|_{\mathrm{F}}^2 \\ + \mu\sum_{i=1}^{s_3}\sum_{j=1}^{r_3}\left\|\mathbf{U}_{i,j}\right\|_2 + \left\langle\Lambda, \mathbf{B}\hat{\mathbf{X}}_3 + \mathbf{C}\mathbf{U}\right\rangle \\ + \frac{\beta}{2}\left\|\beta\hat{\mathbf{X}}_3 + \mathbf{C}\mathbf{U}\right\|_{\mathrm{F}}^2 \end{aligned} \quad (28)$$

where $\mathbf{B}\hat{\mathbf{X}}_3 + \mathbf{C}\mathbf{U} := [\mathbf{D}_1, \mathbf{D}_2]^T\hat{\mathbf{X}}_3 - \hat{\mathbf{I}}_{2s_3\times 2s_3}[\mathbf{U}_1, \mathbf{U}_2]^T = \mathbf{0}_{2s_3\times r_3}$ is a convenient form of the constraints in (27), and $\hat{\mathbf{I}}_{i\times i}$ is the i-by-i identity matrix; $s_n = \Pi_{j\neq n} I_j$; $\Lambda = (\Lambda_1, \Lambda_2)^T$; $\beta > 0$ is the penalty parameter. Then, (28) can be solved by alternately iterating the three variables $\hat{\mathbf{X}}_3$, $\mathbf{U}$, and Λ. Specifically, let p denote the iteration indicator for solving problem (27). With other variables fixed, for the $\mathbf{X}_3$ subproblem, we have

$$\hat{\mathbf{X}}_3^{k+1,p+1} = \arg\min_{\hat{\mathbf{X}}_3} \frac{1}{2}\left\|\hat{\mathbf{Y}}_{(3)}^k - \hat{\mathbf{X}}_3\hat{\mathbf{A}}_3^k\right\|_{\mathrm{F}}^2 + \frac{\rho}{2}\left\|\hat{\mathbf{X}}_3 - \hat{\mathbf{O}}_3^k\right\|_{\mathrm{F}}^2 + \left\langle\Lambda^p, \mathbf{B}\hat{\mathbf{X}}_3 + \mathbf{C}\mathbf{U}^p\right\rangle + \frac{\beta}{2}\left\|\mathbf{B}\hat{\mathbf{X}}_3 + \mathbf{C}\mathbf{U}^p\right\|_{\mathrm{F}}^2. \quad (29)$$

Then, the solution of (29) can be obtained by using the classical Sylvester matrix equation

$$\hat{\mathbf{X}}_3\left(\hat{\mathbf{A}}_3^k(\hat{\mathbf{A}}_3^k)^T\right) + \beta\mathbf{B}^T\mathbf{B}\hat{\mathbf{X}}_3 + \rho\hat{\mathbf{X}}_3 = \rho\hat{\mathbf{O}}_3^k + \hat{\mathbf{Y}}_{(3)}^k(\hat{\mathbf{A}}_3^k)^T - \mathbf{B}^T\Lambda^p - \beta\mathbf{B}^T\mathbf{C}\mathbf{U}^p. \quad (30)$$

By using the Kronecker product notations, (30) can be rewritten as follows:

$$\left(\hat{\mathbf{A}}_3^k(\hat{\mathbf{A}}_3^k)^T \otimes \mathbf{I} + \beta\mathbf{I}\otimes\mathbf{B}^T\mathbf{B} + \rho_1\mathbf{I}\otimes\mathbf{I}\right)\mathrm{vec}(\hat{\mathbf{X}}_3) = \mathrm{vec}\left(\rho\hat{\mathbf{O}}_3^k + \hat{\mathbf{Y}}_{(3)}^k(\hat{\mathbf{A}}_{(3)}^k)^T - \mathbf{B}^T\Lambda^p - \beta\mathbf{B}^T\mathbf{C}\mathbf{U}^p\right) \quad (31)$$

where vec(.) refers to a vector by lexicographical ordering of the entries in a matrix. Using SVD of $\hat{\mathbf{A}}_3^k$, i.e., $\hat{\mathbf{A}}_3^k = \mathbf{P}\Sigma\mathbf{Q}^*$, and the Fourier decomposition of $\mathbf{B}^T\mathbf{B}$ with periodic boundary condition, i.e., $\mathbf{B}^T\mathbf{B} = \mathbf{F}^*\Psi^2\mathbf{F}$, we can solve problem (31) efficiently. Then, (31) can be rewritten as follows:

$$\left(\mathbf{P}\otimes\mathbf{F}^*\right)\left(\Sigma^2\otimes\mathbf{I} + \beta\mathbf{I}\otimes\Psi^2 + \rho\mathbf{I}\otimes\mathbf{I}\left(\mathbf{P}^*\otimes\mathbf{F}\right)\mathrm{vec}\left(\hat{\mathbf{X}}_3\right)\right) = \mathrm{vec}\left(\rho\hat{\mathbf{O}}_3^k + \hat{\mathbf{Y}}_{(3)}^k\left(\hat{\mathbf{A}}_3^k\right)^T - \mathbf{B}^T\Lambda^p - \beta\mathbf{B}^T\mathbf{C}\mathbf{U}^p\right). \quad (32)$$

The solution $\mathrm{vec}(\hat{\mathbf{X}}_3)$ is explicitly expressed as follows:

$$\mathrm{vec}\left(\hat{\mathbf{X}}_3\right) = \left(\mathbf{P}\otimes\mathbf{F}^*\right)\left(\Sigma^2\otimes\mathbf{I} + \beta\mathbf{I}\otimes\Psi^2 + \rho\mathbf{I}\otimes\mathbf{I}\right)^{-1}\left(\mathbf{P}^*\otimes\mathbf{F}\right) \cdot \mathrm{vec}\left(\rho\hat{\mathbf{O}}_3^k + \hat{\mathbf{Y}}_{(3)}^k\left(\hat{\mathbf{A}}_3^k\right)^T - \mathbf{B}^T\Lambda^p - \beta\mathbf{B}^T\mathbf{C}\mathbf{U}^p\right). \quad (33)$$

With other variables fixed, the minimization subproblem for $\mathbf{U}$ can be deduced from (28) as follows:

$$\mathbf{U}^{p+1} = \arg\min_{\mathbf{U}} \mu\sum_{i=1}^{s_3}\sum_{j=1}^{r_3}\left\|\mathbf{U}_{i,j}\right\|_2 + \frac{\beta}{2}\left\|\mathbf{B}\hat{\mathbf{X}}_3^{k+1,p+1} + \mathbf{C}\mathbf{U} + \frac{\Lambda^p}{\beta}\right\|_{\mathrm{F}}^2. \quad (34)$$

Its solution can be transformed into solving s_3r_3 two-variable minimization problems independently as follows:

$$\begin{aligned}\arg\min_{\mathbf{U}_1,\mathbf{U}_2} \mu\sqrt{\left|(\mathbf{U}_1)_{i,j}\right|^2 + \left|(\mathbf{U}_2)_{i,j}\right|^2} \\ + \frac{\beta}{2}\left[(\mathbf{U}_1)_{i,j} - \left(\mathbf{D}_1\hat{\mathbf{X}}_3^{k+1,p+1}\right)_{i,j} - \frac{1}{\beta}(\Lambda_1^p)_{i,j}\right]^2 \\ + \frac{\beta}{2}\left[(\mathbf{U}_2)_{i,j} - \left(\mathbf{D}_2\hat{\mathbf{X}}_3^{k+1,p+1}\right)_{i,j} - \frac{1}{\beta}(\Lambda_2^p)_{i,j}\right]^2. \end{aligned} \quad (35)$$

The solution of (35) can be obtained by using the well-known 2-D shrinkage formula

$$\left[(\mathbf{U}_1)_{i,j}, (\mathbf{U}_2)_{i,j}\right] = \max\left\{\left\|\mathbf{T}_{i,j}\right\|_2 - \frac{\mu}{\beta}, 0\right\}\frac{\mathbf{T}_{i,j}}{\left\|\mathbf{T}_{i,j}\right\|_2} \quad (36)$$

where $\mathbf{T}_{i,j} = [\mathbf{D}_1^{\Lambda_1}, \mathbf{D}_2^{\Lambda_2}]$, with

$$\begin{cases}\mathbf{D}_1^{\Lambda_1} = \left(\mathbf{D}_1\hat{\mathbf{X}}_3^{k+1,p+1}\right)_{i,j} + \frac{1}{\beta}(\Lambda_1^p)_{i,j} \\ \mathbf{D}_2^{\Lambda_2} = \left(\mathbf{D}_2\hat{\mathbf{X}}_3^{k+1,p+1}\right)_{i,j} + \frac{1}{\beta}(\Lambda_2^p)_{i,j}\end{cases} \quad (37)$$

$1 \le i \le s_3, 1 \le j \le r_3$; we assign $0\cdot(0/0) = 0$, as stated in [40].

After solving the two subproblems with respect to $\hat{\mathbf{X}}_3$ and $\mathbf{U}$, the Lagrangian multipliers $\Lambda = (\Lambda_1, \Lambda_2)^T$ can be updated in parallel as follows:

$$\Lambda^{p+1} = \Lambda^p + \beta\left(\mathbf{B}\hat{\mathbf{X}}_3^{k+1,p+1} + C\mathbf{U}^{p+1}\right). \quad (38)$$

Authorized licensed use limited to: University of Gent. Downloaded on August 08,2023 at 08:45:04 UTC from IEEE Xplore. Restrictions apply.

This article has been accepted for inclusion in a future issue of this journal. Content is final as presented, with the exception of pagination.

2) Update $\mathbf{A}_n$ With Fixing Others: By introducing an auxiliary variable $\mathbf{A}_n = \mathbf{J}_n$, the $\mathbf{A}_n$ subproblem can be rewritten as follows:

$$\begin{aligned}\arg\min_{\mathbf{A}_n,\mathbf{J}_n}\sum_{n=1}^{N}\Big(&\frac{\alpha_n}{2}\left\|\mathbf{Y}_{(n)}-\mathbf{A}_n\mathbf{X}_n\right\|_{\mathrm{F}}^2+\lambda_n\|\mathbf{J}_n\|_*\\&+\frac{\rho_n}{2}\left\|\mathbf{A}_n-\mathbf{A}_n^k\right\|_{\mathrm{F}}^2+\left\langle\Gamma_n^{\mathbf{A}},\mathbf{A}_n-\mathbf{J}_n\right\rangle\\&+\frac{\rho_n}{2}\|\mathbf{A}_n-\mathbf{J}_n\|_{\mathrm{F}}^2\Big)\end{aligned}\tag{39}$$

where $\Gamma_n^{\mathbf{A}}$ is the Lagrangian multiplier. First, $\mathbf{J}_n$ can also be obtained by SVT operator (12)

$$\mathbf{J}_n^{k+1}=\mathrm{SH}_{\frac{\lambda_n}{\rho_n}}\left(\mathbf{A}_n^k+\Gamma_n^{\mathbf{A}}/\rho_n\right),\quad n=1,2,\ldots,N.\tag{40}$$

Second, with other variables fixed, the minimization subproblem for $\mathbf{A}_n$ can be deduced from (39) as follows:

$$\begin{aligned}\mathbf{A}_n^{k+1}=\arg\min_{\mathbf{A}_n}\sum_{n=1}^{N}\Bigg(&\frac{\alpha_n}{2}\left\|\mathbf{Y}_{(n)}-\mathbf{A}_n\mathbf{X}_n\right\|_{\mathrm{F}}^2\\&+\rho_n\left\|\mathbf{A}_n-\frac{\mathbf{J}_n^{k+1}-\Gamma_n^{\mathbf{A}}/\rho_n+\mathbf{A}_n^k}{2}\right\|_{\mathrm{F}}^2\Bigg).\end{aligned}\tag{41}$$

It is also convex and has the following closed-form solution:

$$\begin{aligned}\mathbf{A}_n^{k+1}=&\left(\mathbf{X}_{(n)}^k\left(\mathbf{X}_n^{k+1}\right)^T+2\rho_n\left(\frac{\mathbf{J}_n^{k+1}-\Gamma_n^{\mathbf{A}}/\rho_n+\mathbf{A}_n^k}{2}\right)\right)\\&\times\left(\mathbf{X}_n^{k+1}\left(\mathbf{X}_n^{k+1}\right)^T+2\rho_n\mathbf{I}_n\right)^{\dagger},\quad n=1,2,\ldots,N.\end{aligned}\tag{42}$$

Finally, the Lagrangian multiplier can be updated by the following equations:

$$\Gamma_n^{\mathbf{A}}=\Gamma_n^{\mathbf{A}}+\mathbf{A}_n-\mathbf{J}_n.\tag{43}$$

3) Update $\mathcal{Y}$ With Fixing Others: The minimization subproblem for $\mathbf{Y}_{(n)}$ in (18) can be written as follows:

$$\begin{aligned}\mathbf{Y}_{(n)}^{k+1}=\arg\min_{\mathbf{Y}_{(n)}}&\sum_{n=1}^{N}\left(\frac{\alpha_n}{2}\left\|\mathbf{Y}_{(n)}-\mathbf{A}_n\mathbf{X}_n\right\|_{\mathrm{F}}^2+\frac{\rho}{2}\left\|\mathcal{Y}-\mathcal{Y}^k\right\|_{\mathrm{F}}^2\right)\\&\text{s.t.},\ \mathcal{P}_\Omega(\mathcal{Y})=\mathcal{F}.\end{aligned}\tag{44}$$

Then, the update of $\mathcal{Y}_{k+1}$ can be written explicitly as follows:

$$\mathcal{Y}^{k+1}=P_{\Omega^c}\left(\sum_{n=1}^{N}\alpha_n\ \text{fold}_n\left(\frac{\mathbf{A}_n^{k+1}\mathbf{X}_n^{k+1}+\rho_n\mathbf{Y}_{(n)}^k}{1+\rho_n}\right)\right)+\mathcal{F}\tag{45}$$

where $\mathcal{F}$ is the observed data; P_Ω is an operator defined in Section II-C.

Then, the proposed algorithm for the proposed model-1 and model-2 can be summarized as in Algorithms 1 and 2, respectively.

C. Complexity and Convergence Analysis

In this section, we discuss the complexity and convergence of the proposed algorithms.

Algorithm 1 Algorithm for the Proposed Model-1

Require: The observed tensor $\mathcal{F}$; The set of index of observed entries Ω; The given n-rank, $r=(r_1,r_2,r_3)$; stopping criterion ε.

Ensure: The completed tensor.

1: Initialize: $\mathbf{X}_n^0=\mathbf{Z}_n^0=\mathbf{0}$, $\mathbf{A}_n^0=\mathbf{J}_n^0=\mathbf{0}$, $\Gamma_n^{\mathbf{X}}=\mathbf{0}$, $\Gamma_n^{\mathbf{A}}=\mathbf{0}$, $n=1,2,\ldots,N$; $\mu_{\max}=10^6$, $\rho=1.5$, $\mathcal{Y}=\mathcal{P}_\Omega(\mathcal{F})$, and $k=0$.
2: Repeat until convergence:
3: Update $\mathbf{X}$, $\mathbf{Z}$, $\mathbf{A}$, $\mathbf{J}$, $\mathcal{Y}$, $\Gamma^{\mathbf{X}}$, $\Gamma^{\mathbf{A}}$ via
  1st step: Update $\mathbf{Z}_n$ via (21)
  2nd step: Update $\mathbf{X}_n$, $n=1,2,\ldots,N$, via (24)
  3rd step: Update $\mathbf{A}_n$ via (42)
  4th step: Update $\mathbf{J}_n$ via (40)
  5th step: Update $\mathcal{Y}$ via (45)
  6th step: Update the parameter via (22), (43)
4: Check the convergence condition.

Algorithm 2 Algorithm for the Proposed Model-2

Require: The observed tensor $\mathcal{F}$; The set of index of observed entries Ω; The given n-rank, $r=(r_1,r_2,r_3)$; stopping criterion ε.

Ensure: Output: The completed tensor;

1: Initialize: $\mathbf{A}_n^0=\mathbf{J}_n^0=\mathrm{rand}(I_n\times r_n)$, $\mathbf{X}_n^0=\mathbf{Z}_n^0=\mathrm{rand}(r_n\times\prod_{m=1,m\neq n}^{N}I_m)$, $\mathcal{Y}=\mathcal{P}_\Omega(\mathcal{F})$, $\Gamma_n^{\mathbf{X}}=\mathbf{0}$, $\Gamma_n^{\mathbf{A}}=\mathbf{0}$, $n=1,2,\ldots,N$; $\mu_{\max}=10^6$, $\rho=1.5$, $\mathcal{Y}=\mathcal{P}_\Omega(\mathcal{F})$, and $k=0$.
2: **repeat**
  1st step: Update $\mathbf{Z}_n$ via (21)
  2nd step: Update $\mathbf{X}_n$, $n=1,2,4,5,\ldots,N$, via (24)
  3rd step: Update $\mathbf{X}_3$ via
3: **repeat**
  3-1st step: Update $\mathbf{X}_3$ via (33)
  3-2nd step: Update $\mathbf{U}$ via (36)
  3-3rd step: Update Λ via (38)
4: **until** converged
  4th step: Update $\mathbf{J}_n$ via (40)
  5th step: Update $\mathbf{A}_n$ via (42)
  6th step: Update $\mathcal{Y}$ via (45)
  7th step: Update the parameter via (22), (43)
5: **until** converged

1) Complexity Analysis: The cost of computing $\mathbf{X}_n$ is $O(I_nr_n^2+I_nr_ns_n+r_n^2s_n)$; calculating $\mathbf{Z_n}$ has a complexity of $O(s_nr_n^2)$; the complexity of updating $\mathbf{J}_n$ is $O(I_nr_n^2)$; calculating $\mathbf{A}_n$ has a complexity of $O(I_nr_n^2+I_nr_ns_n+r_n^2s_n)$, and calculating $[\mathbf{U}_1,\mathbf{U}_2]$ has a complexity of $O(s_3r_3)$; the complexity of updating $\mathrm{vec}(\hat{\mathbf{X}}_3)$ is $O(2s_3r_3^2+s_3r_3\log s_3)$; calculating $\mathcal{Y}$ has a complexity of $O(r_1I_1s_1+\cdots+r_NI_Ns_N)$. Given that $r_n\ll s_n, I_n$, the total complexities of the proposed model-1 and model-2 are listed in the following equations, respectively

$$O\left(\sum_{n}^{N}I_nr_ns_n\right)\tag{46}$$

$$O\left(I_3r_3s_3+r_3s_3\log s_3+\sum_{n\neq3}I_nr_ns_n\right)\tag{47}$$

Authorized licensed use limited to: University of Gent. Downloaded on August 08,2023 at 08:45:04 UTC from IEEE Xplore. Restrictions apply.

This article has been accepted for inclusion in a future issue of this journal. Content is final as presented, with the exception of pagination.

where $s_n = \Pi_{j\neq n} I_j$. For comparison, the costs of the single-mode-based TNN, PSTNN, and framelet-based Tensor Nuclear Norm (FTNN) (for the third-order tensor) are

$$\mathcal{O}(I_1 I_2 I_3 \log I_3 + I_1 I_2 I_3 \min(I_1, I_2))$$
$$\mathcal{O}\big(I_1 I_2 I_3 \log(I_3) + I_3 \min\big(I_1 I_2^2, I_2 I_1^2\big)\big)$$
$$O(w I_1 I_2 I_3 (I_3 + \min(I_1, I_2)))$$

respectively.

2) Convergence Analysis: In this section, the convergence of the proposed algorithms is proved theoretically by using the BSUM [43]. The BSUM is an alternative inexact block coordinate descent method, which is proposed recently. It is designed for the nonsmooth optimization problem.

Lemma 1 [40], [43]: Given the problem $\arg\min f(x)$, s.t. $x \in \mathcal{X}$, where $\mathcal{X}$ is the feasible set. Assume $h(x, x^{k-1})$ is an approximation of $f(x)$ at the $(k-1)$th iteration, which satisfied the following conditions:

1) $h_i(y_i, y) = f(y) \quad \forall y \in \mathcal{X} \quad \forall i$
2) $h_i(x_i, y) \geq f(y_1, \ldots, y_{i-1}, x_i, y_{i+1}, \ldots, y_n)$
   $\forall x_i \in \mathcal{X}_i \quad \forall y \in \mathcal{X} \quad \forall i_i$
3) $h_i'(x_i, y; d_i)\big|_{x_i = y_i} = f'(y; d), \quad v_i = (0, \ldots, d_i, \ldots, 0)$
   s.t. $y_i + d_i \in \mathcal{X}_i \quad \forall i$
4) $h_i(x_i, y)$ is continuous in $(x_i, y) \quad \forall i$ (48)

where $h_i(x_i, y)$ is the subproblem with respect to the ith block and $f'(y; d)$ is the direction derivative of f at the point y in direction d. Suppose $h_i(x_i, y)$ is quasi-convex in x_i for $i = 1, 2, \ldots, n$. Furthermore, assume that each subproblem $\operatorname{argmin} h_i(x_i, x^{k-1})$, s.t. $x \in \mathcal{X}_i$, has a unique solution for any point $x^{k-1} \in \mathcal{X}$. Then, the iterates generated by the BSUM algorithm converge to the set of coordinatewise minimum of f.

Theorem 1: The iterates generated by (16) converge to the set of coordinatewise minimizers.

Proof: According to the notations in (16) and (18), we give the notions for convenience

$$\begin{cases} g\big(\mathcal{S}, \mathcal{S}^k\big) = f(\mathcal{S}) + \dfrac{\rho}{2}\big\|\mathcal{S} - \mathcal{S}^k\big\|_{\mathrm{F}}^2 \\ g_1\big(\mathbf{X}, \mathcal{S}_1^k\big) = f\big(\mathbf{X}, \mathbf{A}^k, \mathcal{Y}^k\big) + \dfrac{\rho}{2}\big\|\mathbf{X} - \mathbf{X}^k\big\|_{\mathrm{F}}^2 \\ g_2\big(\mathbf{A}, \mathcal{S}_2^k\big) = f\big(\mathbf{X}^{k+1}, \mathbf{A}, \mathcal{Y}^k\big) + \dfrac{\rho}{2}\big\|\mathbf{A} - \mathbf{A}^k\big\|_{\mathrm{F}}^2 \\ g_3\big(\mathcal{Y}, \mathcal{S}_3^k\big) = f\big(\mathbf{X}^{k+1}, \mathbf{A}^{k+1}, \mathcal{Y}\big) + \dfrac{\rho}{2}\big\|\mathcal{Y} - \mathcal{Y}^k\big\|_{\mathrm{F}}^2. \end{cases} \tag{49}$$

It is easy to verify that $g(\mathcal{S}, \mathcal{S}^k)$ is an approximation and a global upper bound of $f(\mathcal{S})$ at the kth iteration, which satisfies the following conditions:

1) $g_i(\mathcal{S}_i, \mathcal{S}) = f(\mathcal{S}) \quad \forall \mathcal{S}, \quad i = 1, 2, 3$
2) $g_i\big(\bar{\mathcal{S}}_i, \mathcal{S}\big) \geq f\big(\mathcal{S}_1, \ldots, \bar{\mathcal{S}}_i, \ldots, \mathcal{S}_3\big)$
   $\forall \bar{\mathcal{S}}_i \quad \forall \mathcal{S}, \quad i = 1, 2, 3$
3) $g_i'\big(\bar{\mathcal{S}}_i, \mathcal{S}; \mathbf{M}_i\big)\big|_{\bar{\mathcal{S}}_i = \mathcal{S}_i} = f'\big(\mathcal{S}; \mathbf{M}^i\big)$
   $\forall \mathbf{M}^i = (0, \ldots, \mathbf{M}_i, \ldots, 0)$
4) $g_i\big(\bar{\mathcal{S}}_i, \mathcal{S}\big)$ is continuous in $\big(\bar{\mathcal{S}}_i, \mathcal{S}\big), \quad i = 1, 2, 3$ (50)

where $\mathcal{S} = (\mathcal{S}_1, \mathcal{S}_2, \mathcal{S}_3) = (\mathbf{X}, \mathbf{A}, \mathcal{Y})$. In addition, the subproblem $g_i (i = 1, 2, 3)$ is strictly convex with respect to $\mathbf{X}$, $\mathbf{A}$, and $\mathcal{Y}$, respectively, and thus, each subproblem has a unique solution. Therefore, all assumptions in Lemma 1 are satisfied. According to the conclusion of Lemma 1, Theorem 1 is valid, and the proposed algorithms are theoretically convergent.

IV. Numerical Experiments

To verify the effectiveness of the proposed model-1 and model-2, we carry out lots of experiments on three types of public tensor data sets, i.e., video, MRI, and HSI, which have been frequently used to interpret the TC performance of different models. Seven different completion models are selected as comparison methods, i.e., TMac [38], TV-based MF-TV method [40], single nuclear norm-based TNN method [22], FTNN [35], partial sum of tubal nuclear norm-based PSTNN method [37], TC-RE [36], and tensor nuclear norm-based total variation (TNTV) (FFT) [34].

To accurately evaluate the performance of the models, we mainly use two types of standards for evaluation. The first is the visual evaluation of the restored data, which is a qualitative evaluation standard. The second is the five quantitative picture quality indices (PQIs), including the peak signal-to-noise ratio (PSNR) [47], structural similarity index (SSIM) [48], feature similarity (FSIM) [49], erreur relative globale adimensionnelle de synthèse (ERGAS) [50], the mean, and the spectral angle mapper (SAM) [51] (only for HSI datasets). The larger the PSNR, SSIM, and FSIM and the smaller the ERGAS and SAM are, the better the restoration performance of the corresponding model is. Since the experimental datasets are all third-order tensors, the PQIs for each frontal slice in the restored tensor are first calculated, and then, the mean of these PQIs is finally used to evaluate the performance of the models. All experiments were performed on MATLAB 2018b, the CPU of the computer is Intel core i7@2.2 GHz, and the RAM is 64 GB.

For a tensor $\mathcal{Y} \in \mathbb{R}^{I_1 \times \cdots \times I_N}$, let S_{number} denote the number of sampled entries in its index set Ω. Then, the sampling ratio (SR) can be defined as follows:

$$\text{SR} = \frac{S_{\text{number}}}{\prod_{n=1}^{N} I_n} \tag{51}$$

where the sampled entries are chosen randomly from a tensor $\mathcal{Y}$ by a uniform distribution. In the proposed algorithms for model-1 and model-2, the inputs include the observed tensor $\mathcal{F} \in \mathbb{R}^{I_1 \times I_2 \times I_3}$, the stopping criteria ϵ, the regularized parameters α, β, λ, and τ, and the penalty parameter β. All parameters are empirically. Specifically, the stopping criterion ϵ and the weights $\alpha_i (i = 1, 2, 3)$ of the proposed model-1 and model-2 are set to be 10^{-5} and $1/3$ for all experiments; the regularization parameter μ and the penalty parameter β for model-2 are set as 0.5 and 10, respectively; finally, the proximal parameter ρ and regularized parameters λ and τ are all set as 0.1 for all experiments of model-1 and model-2.

A. Video

In this part, the proposed model is applied to two video datasets to verify the performance of the model. The two video

Authorized licensed use limited to: University of Gent. Downloaded on August 08,2023 at 08:45:04 UTC from IEEE Xplore. Restrictions apply.

This article has been accepted for inclusion in a future issue of this journal. Content is final as presented, with the exception of pagination.

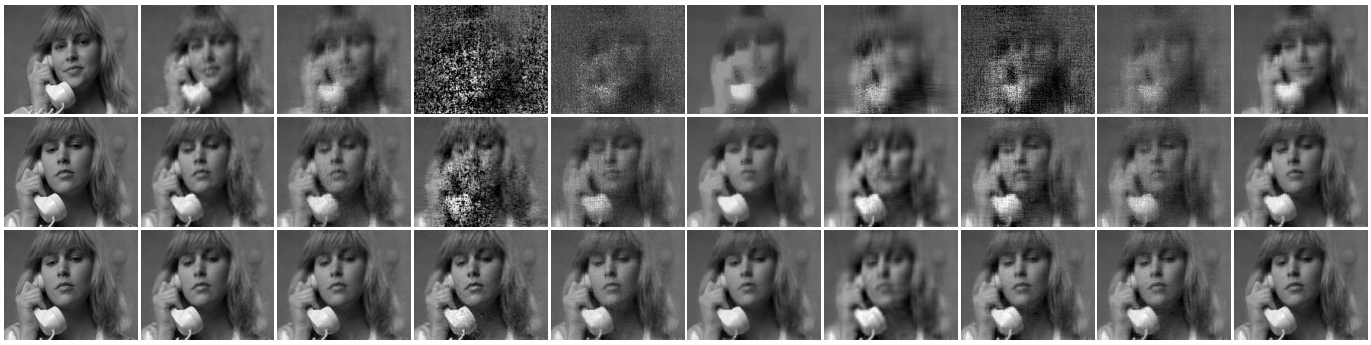


Fig. 4. Slices of the recovered video for "Suzie" by our model-1 and model-2, MF-TV, TC-RE, TNTV, Tmac, PSTNN, FTNN, and TNN. The sampling rates for the first, second, and third rows are 5%, 10%, and 20%, respectively.

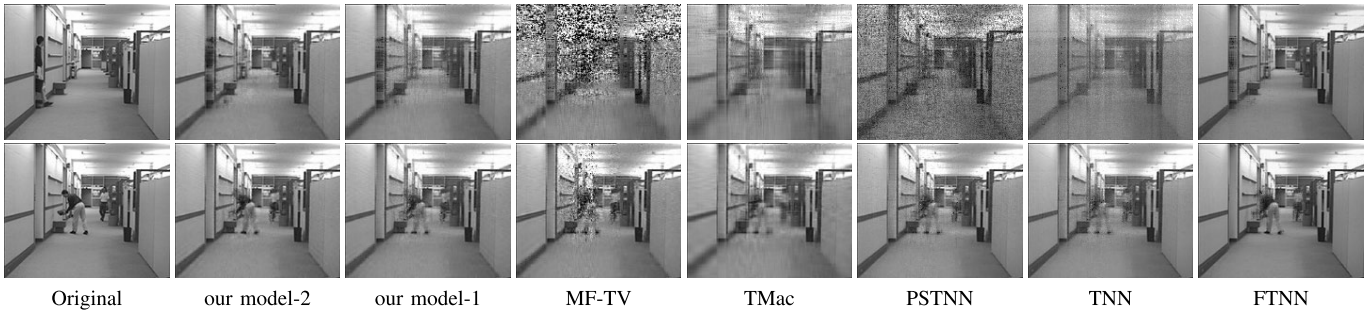


Fig. 5. One slice of the recovered video "Hall" by our model-1 and model-2, MF-TV, Tmac, PSTNN, FTNN, and TNN. The sampling rates of the first and second rows are 5% and 10%, respectively.

TABLE I

AVERAGED PSNR, SSIM, FSIM, AND ERGAS OF THE RECOVERED RESULTS ON VIDEO "SUZIE" BY TMAC, MF-TV, TNN, PSTNN, FTNN, TC-RE, TNTV, AND THE PROPOSED MODEL-1 AND MODEL-2 WITH DIFFERENT SAMPLING RATES. THE BEST VALUE IS HIGHLIGHTED IN BOLD

SR =0.05										
method	noisy	model-2	model-1	MF-TV	TMac	PSTNN	TNN	FTNN	TC-RE	TNTV
PSNR	7.259	**30.268**	26.663	13.801	23.385	17.447	22.005	27.294	16.364	25.090
SSIM	0.009	**0.85**	0.733	0.094	0.622	0.192	0.563	0.465	0.246	0.733
FSIM	0.454	**0.904**	0.852	0.42	0.792	0.59	0.776	0.555	0.643	0.798
ERGAS	1057.282	**76.304**	115.628	501.117	167.927	327.678	194.844	129.27	371.111	138.241
SR = 0.1										
method	noisy	model-2	model-1	MF-TV	TMac	PSTNN	TNN	FTNN	TC-RE	TNTV
PSNR	7.493	**32.272**	30.002	22.356	26.189	26.647	26.032	29.484	25.173	28.736
SSIM	0.014	**0.887**	0.832	0.605	0.74	0.68	0.692	0.585	0.665	0.826
FSIM	0.426	**0.928**	0.899	0.758	0.838	0.843	0.846	0.670	0.839	0.872
ERGAS	1029.096	**60.723**	79.383	196.059	124.369	117.104	124.923	95.472	136.476	92.359
SR = 0.2										
method	nosiy	model-2	model-1	MF-TV	TMac	PSTNN	TNN	FTNN	TC-RE	TNTV
PSNR	8.005	**34.492**	33.745	32.064	27.274	30.566	30.561	32.184	30.683	31.963
SSIM	0.02	**0.921**	0.909	0.872	0.782	0.829	0.831	0.721	0.834	0.897
FSIM	0.391	**0.95**	0.943	0.916	0.853	0.91	0.911	0.788	0.913	0.927
ERGAS	970.285	**46.89**	51.759	66.692	109.627	75.472	75.598	65.322	74.460	63.856

TABLE II

AVERAGED PSNR, SSIM, FSIM, AND ERGAS OF THE RECOVERED RESULTS ON VIDEO "HALL" BY TMAC, MF-TV, TNN, PSTNN, FTNN, AND THE PROPOSED MODEL-1 AND MODEL-2 WITH DIFFERENT SAMPLING RATES. THE BEST VALUE IS HIGHLIGHTED IN BOLD

SR =0.05								
method	noisy	model-2	model-1	MF-TV	TMac	PSTNN	TNN	FTNN
PSNR	4.82	29.571	26.647	13.539	22.101	16.075	20.78	**30.022**
SSIM	0.007	**0.915**	0.862	0.412	0.675	0.36	0.636	0.792
FSIM	0.387	**0.935**	0.899	0.612	0.789	0.672	0.792	0.835
ERGA	1225.779	**73.007**	100.944	452.351	168.866	335.52	195.315	98.14
SR = 0.1								
method	noisy	model-2	model-1	MF-TV	TMac	PSTNN	TNN	FTNN
PSNR	5.055	32.103	30.241	24.855	26.936	29.014	28.433	**32.790**
SSIM	0.013	**0.936**	0.918	0.829	0.854	0.892	0.905	0.854
FSIM	0.393	**0.953**	0.939	0.873	0.888	0.934	0.936	0.889
ERGAS	1193.075	**55.089**	67.967	131.422	97.185	77.395	82.259	59.375
SR = 0.2								
method	noisy	model-2	model-1	MF-TV	TMac	PSTNN	TNN	FTNN
PSNR	5.567	34.045	33.647	33.006	27.648	33.629	33.691	**35.755**
SSIM	0.025	**0.953**	0.952	0.94	0.869	0.961	0.962	0.902
FSIM	0.403	**0.965**	0.964	0.954	0.897	0.973	0.974	0.927
ERGAS	1124.737	**43.939**	46.002	50.971	89.271	46.123	45.851	44.184

datasets are video dataset Suzie and Hall,[1] both of which are colored using the YUV format. Their sizes are 144 × 176 × 150. The sampling rates are set as 5%, 10%, and 20%.

For quantitative comparison, Tables I and II list the PQIs of all the compared models in the three sampling rates. The best results for each PQI are marked in bold. It is clear from Tables I and II that in all SR cases, our model-2 obtains the best results, and our model-1 obtains suboptimal results compared with other methods. For visual evaluation, we show one frontal slice of the recovered results with different random sampling rates in Figs. 4 and 5. Compared with other models, it can be seen that the results of our models are closest to the original reference images, especially at low sampling rates. It is interested that as SR was low (e.g., SR = 10% or 5%), the proposed models with multimodes correlation performed even much better than its counterparts. Specifically, as shown in Fig. 5, when the sampling rate is 0.05 and 0.1, the advantages of the proposed models are most obvious.

[1] http://trace.eas.asu.edu/yuv/

Authorized licensed use limited to: University of Gent. Downloaded on August 08,2023 at 08:45:04 UTC from IEEE Xplore. Restrictions apply.

This article has been accepted for inclusion in a future issue of this journal. Content is final as presented, with the exception of pagination.

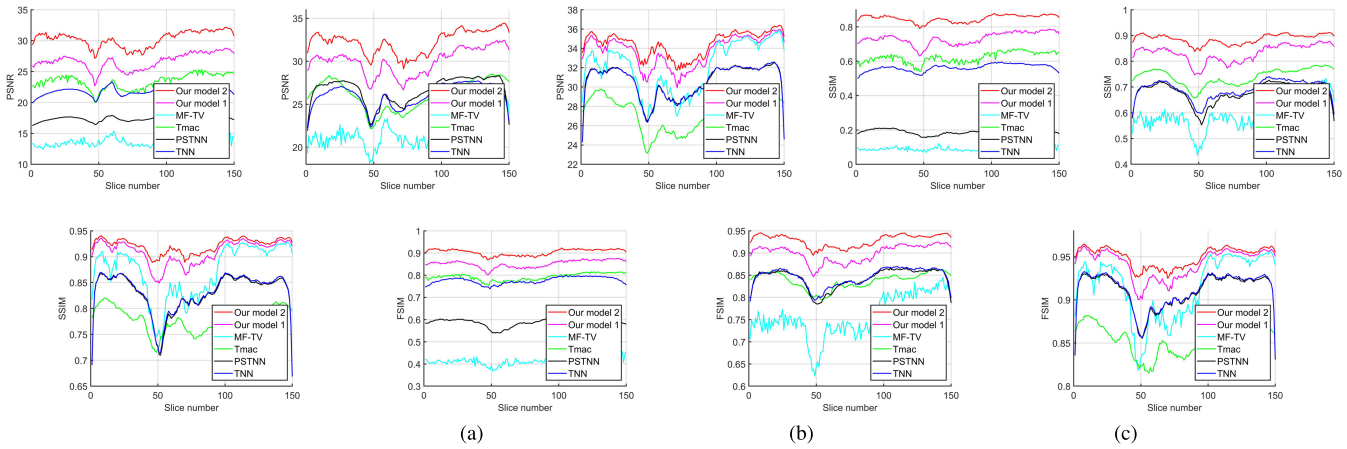


Fig. 6. PSNR, SSIM, and FSIM of the recovered video "Suzie" by MF-TV, Tmac, TNN, PSTNN, and our model-1 and model-2 for all slices, respectively. (a) SR = 0.05. (b) SR = 0.1. (c) SR = 0.2.

The proposed models restore most of the structural information of the lady in the video, while the image restored by the competitive method contains only the outline of the character. At a higher sampling rate, as shown in Figs. 4 and 5, the methods recover more texture and detail information then the counterparts, but the gap between them is much small than that of SR = 5% and 10%. Such an observation is further highlighted in Fig. 6, which displays the PSNR, SSIM, and FSIM of each slice.

This could be explained by the case that all slices among third mode might have missing values at common locations (i.e., some mode-3 fibers were entirely missing or missed most of them) as SR was low, and in this case, the first and the second-mode unfolding had some columns or rows not missing most of their elements, which would help to recover the missing mode-3 fibers via the proposed multimodes regularization among these two modes, while the models only employ single mode-3 correlation among the third mode performed worse. From the perspective of theoretical analysis, as the SR is low, the ill-posedness of the completion problem is much greater than that of higher SR owing to the increased number of elements sampling. In this case, one needs much more prior to compact the solution space to get a promising solution. Therefore, applying the proposed multimodes-based models produces better results than the models that only employ single-mode correlation or single layer low rankness.

In addition, the experiment results also show that the proposed model also outperforms the single-mode-based TNN, PSTNN, and FTNN with respect to quantitative and qualitative comparison, which verifies that the multimodes correlation is effective and efficient.

B. MRI

In this part, to further verify the versatility of our models for different datasets, the proposed models are applied to the MRI dataset, i.e., the cubical MRI data.[2] The size of the dataset is 150 × 150 × 181. The sampling rates are set as 5%, 10%, 20%, and 30%.

[2]http://brainweb.bic.mni.mcgill.ca/brainweb/selection_normal.html

TABLE III

AVERAGED PSNR, SSIM, FSIM, AND ERGAS OF THE RECOVERED RESULTS ON MRI BY TMAC, MF-TV, TNN, PSTNN, FTNN, TC-RE, TNTV, AND THE PROPOSED MODEL-1 ANDMODEL-2 WITH DIFFERENT SAMPLING RATES. THE BEST VALUE IS HIGHLIGHTED IN BOLD

SR =0.05										
method	noisy	model-2	model-1	MF-TV	TMac	PSTNN	TNN	FTNN	TC-RE	TNTV
PSNR	10.258	**24.048**	23.54	12.332	20.51	15.859	18.218	22.540	17.304	20.498
SSIM	0.228	**0.696**	0.597	0.099	0.45	0.224	0.27	0.508	0.278	0.622
FSIM	0.473	**0.817**	0.791	0.52	0.711	0.642	0.646	0.732	0.654	0.728
ERGAS	1030.203	**212.967**	230.079	814.747	339.385	545.77	268.839	434.774	527.093	378.386
SR = 0.1										
method	noisy	model-2	model-1	MF-TV	TMac	PSTNN	TNN	FTNN	TC-RE	TNTV
PSNR	10.492	**31.9**	28.085	15.406	21.411	22.061	22.535	27.641	22.624	24.704
SSIM	0.241	**0.919**	0.798	0.25	0.531	0.482	0.536	0.805	0.508	0.793
FSIM	0.511	**0.932**	0.879	0.587	0.732	0.764	0.78	0.885	0.756	0.835
ERGAS	1002.8	**86.415**	134.58	584.827	308.655	275.473	266.753	165.366	296.484	235.829
SR = 0.2										
method	noisy	model-2	model-1	MF-TV	TMac	PSTNN	TNN	FTNN	TC-RE	TNTV
PSNR	11.003	**35.842**	34.166	27.062	22.33	29.152	28.571	31.783	29.768	29.452
SSIM	0.271	**0.963**	0.941	0.737	0.586	0.804	0.802	0.907	0.797	0.909
FSIM	0.564	**0.965**	0.954	0.84	0.754	0.895	0.891	0.938	0.881	0.919
ERGAS	945.583	**54.522**	66.369	173.636	276.269	127.133	136.182	100.44	133.927	136.896
SR = 0.3										
method	noisy	model-2	model-1	MF-TV	TMac	PSTNN	TNN	FTNN	TC-RE	TNTV
PSNR	11.582	**37.991**	37.301	36.355	23.077	32.608	32.481	34.804	33.145	32.300
SSIM	0.303	**0.977**	0.971	0.954	0.625	0.895	0.89	0.949	0.887	0.947
FSIM	0.597	**0.978**	0.975	0.962	0.773	0.939	0.939	0.963	0.924	0.950
ERGAS	884.608	**42.534**	46.165	52.449	252.057	85.845	87.312	70.542	90.893	98.515

Table III summarizes the PQIs of the recovered results at the four sampling rates in the MRI dataset. It can be clearly found that our proposed models achieve higher PQIs than the comparative models. For visual comparison, at a sampling rate of 0.1, Fig. 7 shows the gray-scale images of the original MRI data, the sampled data, and the different recovered results. It can be seen that our models can better retain the local details and texture information of the images and effectively restore the main structure of the image. Therefore, one can see that the recovered data obtained by our models have the best visual evaluation. Also, the same advantage of our models can also be seen in Fig. 8, which illustrates the PSNR, SSIM, and FSIM values slice by slice in all sampling rates.

C. Hyperspectral Image

In this section, we select two HSI data to apply simulated experiments. The first dataset is the Pavia City Centre,[3]

[3]http://www.ehu.es/ccwintco/index.php/Hyperspectral_Remote_Sensing_Scenes

Authorized licensed use limited to: University of Gent. Downloaded on August 08,2023 at 08:45:04 UTC from IEEE Xplore. Restrictions apply.

This article has been accepted for inclusion in a future issue of this journal. Content is final as presented, with the exception of pagination.

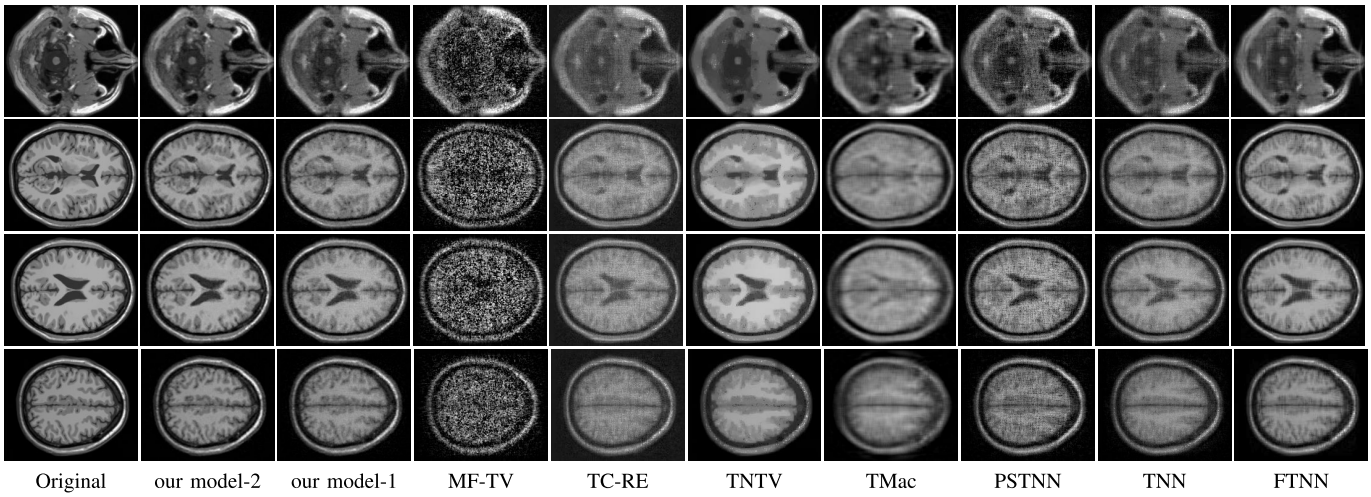


Fig. 7. Slices of the recovered MRI by our model-1 and model-2, MF-TV, TMac, PSTNN, FTNN, TNN, TC-RE, and TNTV. The sampling rate is 10%.

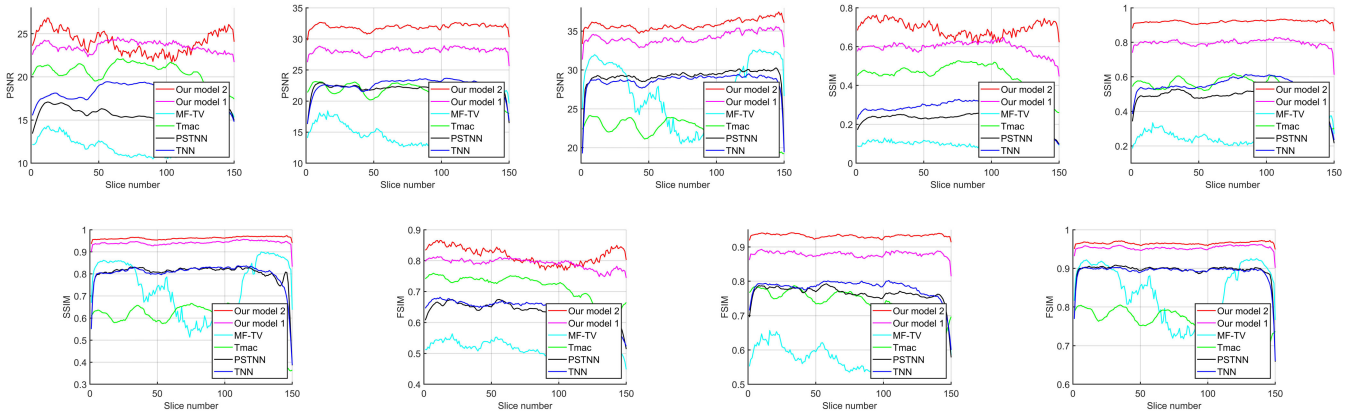


Fig. 8. PSNR, SSIM, and FSIM of the recovered MRI by MF-TV, TMac, TNN, PSTNN, and our model-1 and model-2 for all slices, respectively. (a) SR = 0.05. (b) SR = 0.1. (c) SR = 0.2.

which was filmed by the reflection optical system imaging spectrometer (ROSIS-03). Its size is 1096 × 1096, with a total of 102 bands. Because some of the bands in the Pavia City Centre dataset are heavily polluted by noise, they cannot be used as a reference for restoration results. Therefore, this part of the heavily polluted data has been removed. Due to space limitations, we select data with a spatial size of 200 × 200 and a total of 80 bands for simulated experiments in this part. The second dataset is the Airborne Visible/Infrared Imaging Spectrometer (AVIRIS) Cuprite data.[4] Its size is 150 × 150 × 210. The sampling rate is set to 0.025, 0.05, and 0.1.

Tables IV and V list the PQIs of the results restored by the proposed models and the competition model at three sampling rates. Fig. 9 shows one slice of the recovered "Cuprite" for all methods at a sampling rate of 0.05. Fig. 10 shows one slice of the recovered "Pavia" for all methods at the sampling rates of 0.025 and 0.05. It can be clearly seen that the two proposed methods not only obtain the higher PQIs, but also recover the more structure information of the image, and restore more spatial details than comparison methods, especially at low sampling rates. Therefore, one can see that the recovered data obtained by our models have the best visual evaluation and PQIs.

D. Other Applications and Comparison With Deep Learning

In this section, we apply the proposed model to general tensor completion problems, i.e., *color video inpainting*, *destriping*, and *cloud removal*, on dataset Akiyo,[5] NASA's HSIs Ottawa, and Sentinel-2 MSI multitemporal data,[6] respectively. Addition to the aforementioned state of the arts (SOTA), Smooth matrix factorization based low-rank tensor completion model (SMF-LRTC) [52], small data-based adaptive moment estimation (sdADAM) [53], and deep learning-based ADMM-ADAM [54] are selected for comparison. Figs. 11–13 provide the visual comparison, and one can see that the proposed model also shows comparable performance.

E. Ablation Studies and Running Time Analysis

In this section, we evaluate the components of the proposed models, by conducting experiments on video "Suzie" with

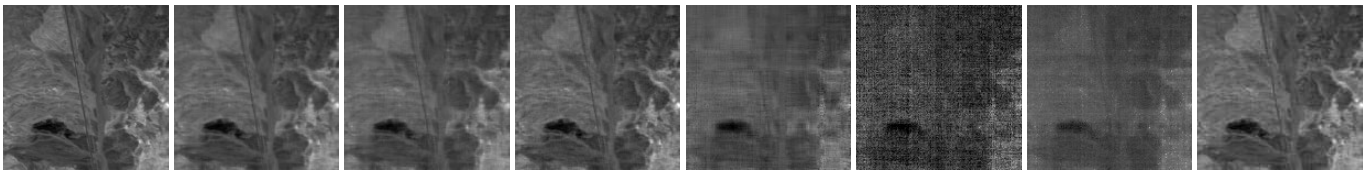
[4]http://aviris.jpl.nasa.gov/html/aviris.freedata.html

[5]http://trace.eas.asu.edu/yuv/

[6]https://drive.google.com/file/d/1LlvUKtUWAKoF6R0igbREwvP2

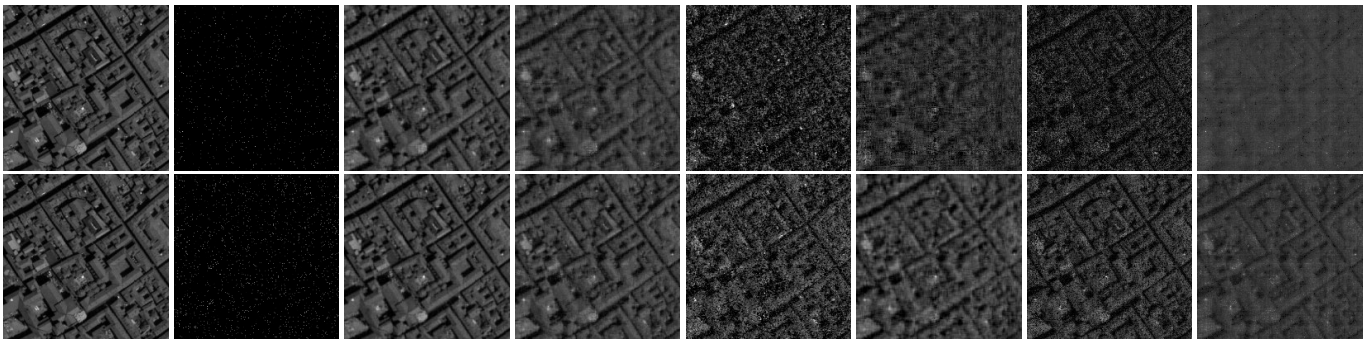
Authorized licensed use limited to: University of Gent. Downloaded on August 08,2023 at 08:45:04 UTC from IEEE Xplore. Restrictions apply.

This article has been accepted for inclusion in a future issue of this journal. Content is final as presented, with the exception of pagination.



(a) (b) (c) (d) (e) (f) (g) (h)

Fig. 9. One slice of the recovered HSI "Cuprite" by our model-1 and model-2, MF-TV, TMac, PSTNN, and TNN. The sampling rate is 5%. (a) Original. (b) Our model-2. (c) Our model-1. (d) MF-TV. (e) TMac. (f) PSTNN. (g) TNN. (h) FTNN.



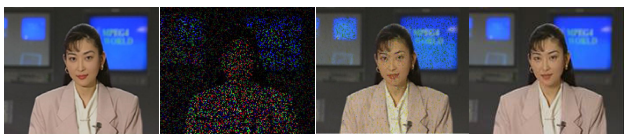
Original 95% Masked our model-2 our model-1 MF-TV TMac PSTNN TNN

Fig. 10. Slices of the recovered HSI "Pavia" by our model-1 and model-2, MF-TV, TMac, PSTNN, and TNN. The sampling rates of the first and second rows are 2.5% and 5%, respectively.

TABLE IV

AVERAGED PSNR, SSIM, FSIM, ERGA, AND SAM OF THE RECOVERED RESULTS ON HSI "CUPRITE" BY TMAC, MF-TV, TNN, PSTNN, AND THE PROPOSED MODEL-1 AND MODEL-2 WITH DIFFERENT SAMPLING RATES. THE BEST VALUE IS HIGHLIGHTED IN BOLD

SR =0.025							
method	noisy	model-2	model-1	MF-TV	TMac	PSTNN	TNN
PSNR	7.666	**34.983**	31.985	26.115	21.25	13.387	22.783
SSIM	0.007	**0.877**	0.807	0.539	0.412	0.124	0.554
FSIM	0.48	**0.91**	0.861	0.765	0.755	0.613	0.775
ERGAS	1043.633	**47.3**	64.636	237.074	235.594	539.574	245.333
MSAM	81.221	**1.483**	1.833	12.913	7.842	17.98	9.156
SR = 0.05							
method	noisy	model-2	model-1	MF-TV	TMac	PSTNN	TNN
PSNR	7.779	**38.433**	35.402	34.684	28.945	20.621	26.579
SSIM	0.01	**0.936**	0.893	0.845	0.712	0.31	0.663
FSIM	0.471	**0.959**	0.928	0.915	0.846	0.735	0.836
ERGAS	1030.139	**34.53**	45.581	89.372	93.352	234.445	154.292
MSAM	77.268	**1.225**	1.481	4.386	3.278	7.886	5.413
SR = 0.1							
method	noisy	model-2	model-1	MF-TV	TMac	PSTNN	TNN
PSNR	8.013	**41.182**	39.084	40.888	35.627	35.51	35.015
SSIM	0.014	**0.961**	0.946	0.957	0.885	0.907	0.897
FSIM	0.451	**0.979**	0.968	0.978	0.931	0.951	0.943
ERGAS	1002.75	**28.338**	33.934	34.263	44.518	54.421	57.537
MSAM	71.695	**1.098**	1.25	1.46	1.445	2.072	2.192



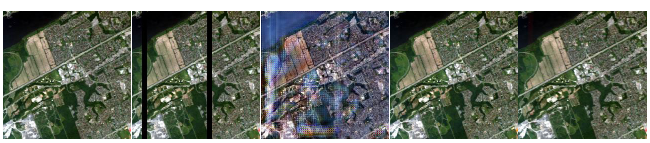
(a) (b) (c) (d)

Fig. 11. One slice (first) of completed color video "Akiyo" by our model-2 and SMF-LRTC. Sampling rate is 15%. (a) Original. (b) 85% masked. (c) SMF-LRTC. (d) Our model-2.

TABLE V

AVERAGED PSNR, SSIM, FSIM, ERGA, AND SAM OF THE RECOVERED RESULTS ON HSI "PAVIA" BY TMAC, MF-TV, TNN, PSTNN, AND THE PROPOSED MODEL-1 AND MODEL-2 WITH DIFFERENT SAMPLING RATES. THE BEST VALUE IS HIGHLIGHTED IN BOLD

SR =0.025							
method	noisy	model-2	model-1	MF-TV	TMac	PSTNN	TNN
PSNR	13.388	**29.353**	24.781	20.132	20.765	17.39	19.984
SSIM	0.014	**0.859**	0.654	0.385	0.379	0.288	0.344
FSIM	0.436	**0.905**	0.801	0.726	0.717	0.705	0.639
ERGAS	787.86	**124.945**	211.791	450.292	344.451	496.92	369.941
MSAM	81.947	**6.612**	8.622	36.188	16.917	34.622	14.16
SR = 0.05							
method	noisy	model-2	model-1	MF-TV	TMac	PSTNN	TNN
PSNR	13.5	**33.066**	28.46	25.442	24.6	21.028	22.557
SSIM	0.025	**0.938**	0.832	0.643	0.64	0.512	0.538
FSIM	0.469	**0.958**	0.893	0.835	0.798	0.791	0.752
ERGAS	777.776	**81.615**	139.446	316.6	216.234	326.121	276.113
MSAM	77.699	**5.024**	7.267	26.414	10.31	22.871	13.08
SR = 0.1							
method	noisy	model-2	model-1	MF-TV	TMac	PSTNN	TNN
PSNR	13.736	**37.347**	32.818	36.064	26.523	29.518	27.363
SSIM	0.046	**0.976**	0.932	0.938	0.737	0.857	0.806
FSIM	0.516	**0.985**	0.954	0.965	0.832	0.923	0.889
ERGAS	756.907	**50.103**	85.931	93.891	172.184	132.084	163.529
MSAM	71.908	**3.727**	5.896	9.397	8.871	11.236	10.825



Original Masked sdADAM Deep ADMM Our model-2

Fig. 12. Visual comparison (18th, 8th, and 2nd bands) of deep ADMM: ADMM-ADAM [54], sdADAM [53], and the proposed model-2 on the Ottawa dataset.

SR = 0.15. Table VI and Fig. 14 provide the PSNR, SSIM, FSIM, ERGAS, and visual comparison of the ablation studies, respectively; one can observe that the bilayer LR can reconstruct much more structure information than single

Authorized licensed use limited to: University of Gent. Downloaded on August 08,2023 at 08:45:04 UTC from IEEE Xplore. Restrictions apply.

This article has been accepted for inclusion in a future issue of this journal. Content is final as presented, with the exception of pagination.

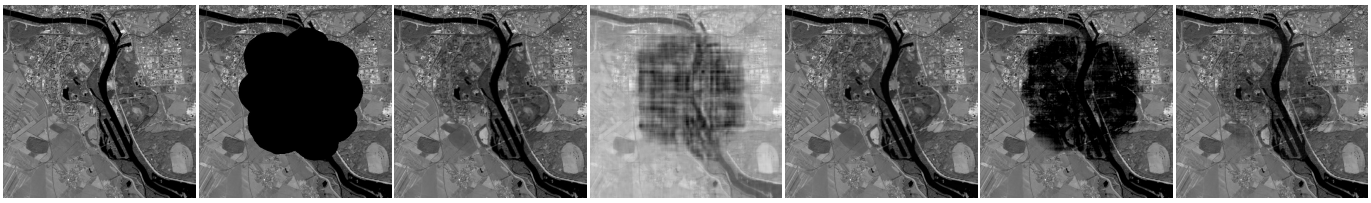


Fig. 13. Sentinel-2 MSI multitemporal data sequence cloud removal experiments (20-m spatial resolution; 10 × 10 km; five temporal images) over Mechelen in Belgium.

TABLE VI

ABLATION STUDY ON VIDEO. EACH COMPONENT IN THE PROPOSED MODELS HAS AN EVIDENT IMPACT ON FINAL PERFORMANCE

Model	Observation	Single layer LR	Bilayer LR	Bilayer LR + TV
PSNR	7.743	26.847	32.280	33.625
SSIM	0.017	0.767	0.882	0.908
FSIM	0.407	0.846	0.926	0.942
ERGAS	1000.014	115.412	61.446	51.966

TABLE VII

RUNNING TIME (IN SECONDS) ANALYSIS ON THE SUZIE DATASET

Model	TMac	TNN	PSTNN	FTNN	MF-TV	Our model-2
Time	6.02	25.29	28.91	89.06	124.21	112.36



Fig. 14. Visual comparison of the ablation studies, from the single layer LR to bilayer LR and TV-enhanced bilayer LR; the reconstructed tensor is improved step by step.

layer LR, while TV enhances the result of bilayer and results in improved local patches. In addition, Table VII listed the running time (recorded by the built-in time function of MATLAB) of the proposed model-2 and its counterparts, in which the testing data are video Suzie, while the SR = 0.5. One can see that representing additional multimodes correlation needs a computation budget, so the proposed model is slower than single-mode-based models. But, it is a little faster than MF-TV, which also employs multimodes.

V. CONCLUSION

A novel bilayer LR representation model for general N-way ($K \geq 3$) tensors is first defined to exploit the low rankness in spectral domain for all orientations. Furthermore, in order to preserve the local smoothing structure of the target tensors, we introduce the TV regularization into model-1 and propose our model-2. We then adopted them to LR TC and employed BSUM to efficiently solve our models and rigorously demonstrated that our numerical scheme converges to the coordinatewise minimizers. The proposed models have been evaluated on three types of public datasets, which show that our algorithms can recover a variety of LR tensors with significantly fewer samples than the compared methods. In addition, although the bilayer LR boosts the performance and accelerates the convergence speed, it also introduces extra computations. Therefore, in future, we will try to balance the computation and performance.

REFERENCES

[1] Z. Zha, B. Wen, X. Yuan, J. Zhou, C. Zhu, and A. C. Kot, "Low-rankness guided group sparse representation for image restoration," *IEEE Trans. Neural Netw. Learn. Syst.*, early access, Feb. 7, 2022, doi: 10.1109/TNNLS.2022.3144630.

[2] Y. Peng, A. Ganesh, J. Wright, W. Xu, and Y. Ma, "RASL: Robust alignment by sparse and low-rank decomposition for linearly correlated images," *IEEE Trans. Pattern Anal. Mach. Intell.*, vol. 34, no. 11, pp. 2233–2246, Nov. 2012.

[3] L. Zhuang, H. Gao, J. Huang, and N. Yu, "Semi-supervised classification via low rank graph," in *Proc. 6th Int. Conf. Image Graph.*, Aug. 2011, pp. 511–516.

[4] K. A. Patwardhan, G. Sapiro, and M. Bertalmío, "Video inpainting under constrained camera motion," *IEEE Trans. Image Process.*, vol. 16, no. 2, pp. 545–553, Feb. 2007.

[5] J. Yuan, "MRI denoising via sparse tensors with reweighted regularization," *Appl. Math. Model.*, vol. 69, pp. 552–562, May 2019.

[6] J. Xue, Y. Zhao, S. Huang, W. Liao, J. C.-W. Chan, and S. G. Kong, "Multilayer sparsity-based tensor decomposition for low-rank tensor completion," *IEEE Trans. Neural Netw.*, vol. 33, no. 11, pp. 1–15, Jun. 2021.

[7] H. Zeng, X. Xie, W. Kong, S. Cui, and J. Ning, "Hyperspectral image denoising via combined non-local self-similarity and local low-rank regularization," *IEEE Access*, vol. 8, pp. 50190–50208, 2020.

[8] S. Ma, D. Goldfarb, and L. Chen, "Fixed point and Bregman iterative methods for matrix rank minimization," *Math. Program.*, vol. 128, nos. 1–2, pp. 321–353, 2011.

[9] K. C. Toh and S. Yun, "An accelerated proximal gradient algorithm for nuclear norm regularized linear least squares problems," *Pacific J. Optim.*, vol. 6, nos. 615–640, p. 15, 2010.

[10] C. Chen, B. He, and X. Yuan, "Matrix completion via an alternating direction method," *IMA J. Numer. Anal.*, vol. 32, no. 1, pp. 227–245, 2012.

[11] Y. Wu, H. Tan, Y. Li, F. Li, and H. He, "Robust tensor decomposition based on Cauchy distribution and its applications," *Neurocomputing*, vol. 223, pp. 107–117, Feb. 2017.

[12] H. Wang, F. Zhang, J. Wang, T. Huang, J. Huang, and X. Liu, "Generalized nonconvex approach for Low-Tubal-Rank tensor recovery," *IEEE Trans. Neural Netw. Learn. Syst.*, vol. 33, no. 8, pp. 3305–3319, Aug. 2021.

[13] Y. Liu, J. Liu, and C. Zhu, "Low-rank tensor train coefficient array estimation for tensor-on-tensor regression," *IEEE Trans. Neural Netw. Learn. Syst.*, vol. 31, no. 12, pp. 5402–5411, Dec. 2020.

[14] L. Zhang, W. Wei, Q. Shi, C. Shen, A. Van Den Hengel, and Y. Zhang, "Accurate tensor completion via adaptive low-rank representation," *IEEE Trans. Neural Netw. Learn. Syst.*, vol. 31, no. 10, pp. 4170–4184, Oct. 2019.

[15] J. Yu, G. Zhou, W. Sun, and S. Xie, "Robust to rank selection: Low-rank sparse tensor-ring completion," *IEEE Trans. Neural Netw. Learn. Syst.*, early access, Sep. 3, 2021, doi: 10.1109/TNNLS.2021.3106654.

[16] C. Lu, J. Feng, Y. Chen, W. Liu, Z. Lin, and S. Yan, "Tensor robust principal component analysis: Exact recovery of corrupted low-rank tensors via convex optimization," in *Proc. IEEE Conf. Comput. Vis. Pattern Recognit. (CVPR)*, Jun. 2016, pp. 5249–5257.

Authorized licensed use limited to: University of Gent. Downloaded on August 08,2023 at 08:45:04 UTC from IEEE Xplore. Restrictions apply.

This article has been accepted for inclusion in a future issue of this journal. Content is final as presented, with the exception of pagination.

[17] H. Zeng, X. Xie, and J. Ning, "Hyperspectral image denoising via global spatial–spectral total variation regularized nonconvex local low-rank tensor approximation," *Signal Process.*, vol. 178, Jan. 2021, Art. no. 107805.

[18] X. Chen et al., "A generalized model for robust tensor factorization with noise modeling by mixture of Gaussians," *IEEE Trans. Neural Netw. Learn. Syst.*, vol. 29, no. 11, pp. 5380–5393, Nov. 2018.

[19] Z. Xu, F. Yan, and Y. Qi, "Bayesian nonparametric models for multiway data analysis," *IEEE Trans. Pattern Anal. Mach. Intell.*, vol. 37, no. 2, pp. 475–487, Feb. 2015.

[20] Y.-L. Chen, C.-T. Hsu, and H.-Y. M. Liao, "Simultaneous tensor decomposition and completion using factor priors," *IEEE Trans. Pattern Anal. Mach. Intell.*, vol. 36, no. 3, pp. 577–591, Mar. 2013.

[21] O. Semerci, N. Hao, M. E. Kilmer, and E. L. Miller, "Tensor-based formulation and nuclear norm regularization for multienergy computed tomography," *IEEE Trans. Image Process.*, vol. 23, no. 4, pp. 1678–1693, Apr. 2014.

[22] Z. Zhang and S. Aeron, "Exact tensor completion using t-SVD," *IEEE Trans. Signal Process.*, vol. 65, no. 6, pp. 1511–1526, Mar. 2017.

[23] Y. Wu, H. Tan, Y. Li, J. Zhang, and X. Chen, "A fused CP factorization method for incomplete tensors," *IEEE Trans. Neural Netw. Learn. Syst.*, vol. 30, no. 3, pp. 751–764, Jul. 2018.

[24] L. R. Tucker, "Some mathematical notes on three-mode factor analysis," *Psychometrika*, vol. 31, no. 3, pp. 279–311, Feb. 1966.

[25] H. Zeng, X. Xie, H. Cui, Y. Zhao, and J. Ning, "Hyperspectral image restoration via CNN denoiser prior regularized low-rank tensor recovery," *Comput. Vis. Image Understand.*, vols. 197–198, Aug. 2020, Art. no. 103004.

[26] C.-Y. Ko, K. Batselier, L. Daniel, W. Yu, and N. Wong, "Fast and accurate tensor completion with total variation regularized tensor trains," *IEEE Trans. Image Process.*, vol. 29, pp. 6918–6931, 2020.

[27] J. Liu, P. Musialski, P. Wonka, and J. Ye, "Tensor completion for estimating missing values in visual data," *IEEE Trans. Pattern Anal. Mach. Intell.*, vol. 35, no. 1, pp. 208–220, Jan. 2013.

[28] D. Goldfarb and Z. Qin, "Robust low-rank tensor recovery: Models and algorithms," *SIAM J. Matrix Anal. Appl.*, vol. 35, no. 1, pp. 225–253, 2014.

[29] M. E. Kilmer, K. Braman, N. Hao, and R. C. Hoover, "Third-order tensors as operators on matrices: A theoretical and computational framework with applications in imaging," *SIAM J. Matrix Anal. Appl.*, vol. 34, no. 1, pp. 148–172, Feb. 2013.

[30] W. Cao, Y. Wang, C. Yang, X. Chang, Z. Han, and Z. Xu, "Folded-concave penalization approaches to tensor completion," *Neurocomputing*, vol. 152, pp. 261–273, Mar. 2015.

[31] Q. Zhao et al., "A novel sparsity measure for tensor recovery," in *Proc. IEEE Int. Conf. Comput. Vis. (ICCV)*, Dec. 2015, pp. 271–279.

[32] J. Xue, Y. Zhao, W. Liao, and J. C.-W. Chan, "Nonconvex tensor rank minimization and its applications to tensor recovery," *Inf. Sci.*, vol. 503, pp. 109–128, Nov. 2019.

[33] H. Zeng, X. Xie, H. Cui, H. Yin, and J. Ning, "Hyperspectral image restoration via global L_{1-2} spatial–spectral total variation regularized local low-rank tensor recovery," *IEEE Trans. Geosci. Remote Sens.*, vol. 59, no. 4, pp. 3309–3325, Jul. 2020.

[34] D. Qiu, M. Bai, M. K. Ng, and X. Zhang, "Robust low-rank tensor completion via transformed tensor nuclear norm with total variation regularization," *Neurocomputing*, vol. 435, pp. 197–215, May 2021.

[35] T.-X. Jiang, M. K. Ng, X.-L. Zhao, and T.-Z. Huang, "Framelet representation of tensor nuclear norm for third-order tensor completion," *IEEE Trans. Image Process.*, vol. 29, pp. 7233–7244, 2020.

[36] Q. Shi, Y.-M. Cheung, and J. Lou, "Robust tensor SVD and recovery with rank estimation," *IEEE Trans. Cybern.*, vol. 52, no. 10, pp. 10667–10682, Oct. 2022.

[37] T.-X. Jiang, T.-Z. Huang, X.-L. Zhao, and L.-J. Deng, "Multi-dimensional imaging data recovery via minimizing the partial sum of tubal nuclear norm," *J. Comput. Appl. Math.*, vol. 372, Jul. 2020, Art. no. 112680.

[38] Y. Xu, R. Hao, W. Yin, and Z. Su, "Parallel matrix factorization for low-rank tensor completion," 2013, *arXiv:1312.1254*.

[39] J. M. Bioucas-Dias et al., "Hyperspectral unmixing overview: Geometrical, statistical, and sparse regression-based approaches," *IEEE J. Sel. Topics Appl. Earth Observ. Remote Sens.*, vol. 5, no. 2, pp. 354–379, Apr. 2012.

[40] T.-Y. Ji, T.-Z. Huang, X.-L. Zhao, T.-H. Ma, and G. Liu, "Tensor completion using total variation and low-rank matrix factorization," *Inf. Sci.*, vol. 326, pp. 243–257, Jan. 2016.

[41] J.-F. Cai, E. J. Candes, and Z. Shen, "A singular value thresholding algorithm for matrix completion,' *SIAM J. Optim.*, vol. 20, no. 4, pp. 1956–1982, 2010.

[42] Y. Wang, J. Peng, Q. Zhao, D. Meng, Y. Leung, and X.-L. Zhao, "Hyperspectral image restoration via total variation regularized low-rank tensor decomposition," *IEEE J. Sel. Topics Appl. Earth Observ. Remote Sens.*, vol. 11, no. 4, pp. 1227–1243, Apr. 2018.

[43] M. Razaviyayn, M. Hong, and Z.-Q. Luo, "A unified convergence analysis of block successive minimization methods for nonsmooth optimization," *SIAM J. Optim.*, vol. 23, no. 2, pp. 1126–1153, Sep. 2012.

[44] A. C. Sauve, A. O. Hero, W. L. Rogers, S. J. Wilderman, and N. H. Clinthorne, "3D image reconstruction for a Compton SPECT camera model," *IEEE Trans. Nucl. Sci.*, vol. 46, no. 6, pp. 2075–2084, Dec. 1999.

[45] Y. Xu, W. Yin, Z. Wen, and Y. Zhang, "An alternating direction algorithm for matrix completion with nonnegative factors," *Frontiers Math. China*, vol. 7, no. 2, pp. 365–384, 2012.

[46] R. Glowinski, *Lectures on Numerical Methods for Non-Linear Variational Problems*. Berlin, Germany: Springer, 2008.

[47] Q. Huynh-Thu and M. Ghanbari, "Scope of validity of PSNR in image/video quality assessment," *Electron. Lett.*, vol. 44, no. 13, pp. 800–801, Jun. 2008.

[48] Z. Wang, A. C. Bovik, H. R. Sheikh, and E. P. Simoncelli, "Image quality assessment: From error visibility to structural similarity," *IEEE Trans. Image Process.*, vol. 13, no. 4, pp. 600–612, Apr. 2004.

[49] L. Zhang, L. Zhang, X. Mou, and D. Zhang, "FSIM: A feature similarity index for image quality assessment," *IEEE Trans. Image Process.*, vol. 20, no. 8, pp. 2378–2386, Aug. 2011.

[50] L. Wald, *Data Fusion: Definitions and Architectures: Fusion of Images of Different Spatial Resolutions*. Paris, France: Les Presses de l'École des Mines, 2002.

[51] F. A. Kruse, A. B. Lefkoff, and J. B. Dietz, "Expert system-based mineral mapping in northern death valley, California/Nevada, using the airborne visible/infrared imaging spectrometer (AVIRIS)," *Remote Sens. Environ.*, vol. 44, nos. 2–3, pp. 309–336, Jun. 1993.

[52] Y.-B. Zheng, T.-Z. Huang, T.-Y. Ji, X.-L. Zhao, T.-X. Jiang, and T.-H. Ma, "Low-rank tensor completion via smooth matrix factorization," *Appl. Math. Model.*, vol. 70, pp. 677–695, Jun. 2019.

[53] D. P. Kingma and J. Ba, "Adam: A method for stochastic optimization," 2014, *arXiv:1412.6980*.

[54] C.-H. Lin, Y.-C. Lin, and P.-W. Tang, "ADMM-ADAM: A new inverse imaging framework blending the advantages of convex optimization and deep learning," *IEEE Trans. Geosci. Remote Sens.*, vol. 60, pp. 1–16, 2021.



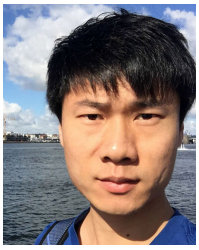
Haijin Zeng (Graduate Student Member, IEEE) received the M.S. degree in applied mathematics from Northwest A&F University, Yangling, China, in 2021. He is currently pursuing the Ph.D. degree with the imec, Ghent University, Ghent, Belgium.

He has authored or coauthored several research articles in his research areas in top-tier journals, including the IEEE TNNLS, the IEEE TGRS, the IEEE TMM, the IEEE TCI, and CVIU. His research interests include image quality improvement, and applications of deep learning and low-rank representation in computational imaging.

Mr. Zeng received the third place in ECCV 2022 mobile intelligent photography and imaging (MIPI) challenge.

Authorized licensed use limited to: University of Gent. Downloaded on August 08,2023 at 08:45:04 UTC from IEEE Xplore. Restrictions apply.

This article has been accepted for inclusion in a future issue of this journal. Content is final as presented, with the exception of pagination.



Shaoguang Huang (Member, IEEE) received the M.S. degree in telecommunication and information system from Shandong University, Jinan, China, in 2015, and the Ph.D. degree in computer science engineering from Ghent University, Ghent, Belgium, in 2019.

He is currently an Associate Professor with the School of Computer Science, China University of Geosciences, Wuhan, China. His research interests include image processing, sparse representation, clustering, hyperspectral image analysis, and machine learning.

Dr. Huang is serving as a Guest Editor for *Remote Sensing*. He is also a Reviewer of international journals, including the IEEE TRANSACTIONS ON CYBERNETICS, the IEEE TRANSACTIONS ON KNOWLEDGE AND DATA ENGINEERING, the IEEE TRANSACTIONS ON GEOSCIENCE AND REMOTE SENSING, the IEEE TRANSACTIONS ON CIRCUITS AND SYSTEMS FOR VIDEO TECHNOLOGY, the IEEE TRANSACTIONS ON BIOMEDICAL CIRCUITS AND SYSTEMS, the IEEE GEOSCIENCE AND REMOTE SENSING LETTERS, *Knowledge-Based Systems, Pattern Recognition, Remote Sensing*, and *Computers and Geosciences*.



Yongyong Chen (Member, IEEE) received the B.S. and M.S. degrees from the Shandong University of Science and Technology, Qingdao, China, in 2014 and 2017, respectively, and the Ph.D. degree from the University of Macau, Macau, China, in 2020.

He is currently an Assistant Professor with the School of Computer Science and Technology, Harbin Institute of Technology, Shenzhen, China. He has authored or coauthored more than 50 research articles in top-tier journals and conferences. His research interests include image processing, data mining, and computer vision.



Sheng Liu received the B.S. degree in information and computer science from Northwest A&F University, Yangling, China, in 2022. He is currently pursuing the M.S. degree with the School of Mathematical Sciences, University of Electronic Science and Technology of China (UESTC), Chengdu, China.

His research interests include tensor modeling and algorithm for high-order data recovery.



Hiêp Q. Luong received the Ph.D. degree in computer science engineering from Ghent University, Ghent, Belgium, in 2009.

He has been working as a Post-Doctoral Researcher and the Project Manager of Image Processing and Interpretation (IPI), an imec Research Group, Ghent University. He is currently a Professor at IPI and leads the Unmanned Aerial Vehicles (UAV) Research Centre, Ghent University. His research interests include image and real-time video processing for various fields, such as high dynamic range (HDR) imaging, (bio) medical imaging, depth and multiview processing, and multisensor fusion for UAV and augmented reality (AR) applications.



Wilfried Philips (Senior Member, IEEE) was born in Aalst, Belgium, in 1966. He received the Diploma degree in electrical engineering and the Ph.D. degree in applied sciences from Ghent University, Ghent, Belgium, in 1989 and 1993, respectively.

He is currently a Senior Full Professor with the Department of Telecommunications and Information Processing, Ghent University, where he heads the Image Processing and Interpretation Research Group. He also leads the activities in image processing and sensor fusion within the research institute imec, Ghent University. He is also a Cofounder of the Senso2Me Company, Antwerpen, Belgium, which provides the Internet of Things Solutions for elderly care. His main research interests include image and video quality improvement and estimation, real-time computer vision, and sensor data processing.

Authorized licensed use limited to: University of Gent. Downloaded on August 08,2023 at 08:45:04 UTC from IEEE Xplore. Restrictions apply.